SANDIA REPORT

SAND2010-6310
Unlimited Release
Printed September 2010

Magnetically Applied Pressure-Shear: A new technique for direct strength measurement at high pressure

(final report for LDRD project 117856)

C. Scott Alexander, James R. Asay, Tom A. Haill, Derek C. Lamppa

Prepared by
Sandia National Laboratories
Albuquerque, New Mexico 87185 and Livermore, California 94550

Sandia National Laboratories is a multi-program laboratory managed and operated by Sandia Corporation, a wholly owned subsidiary of Lockheed Martin Corporation, for the U.S. Department of Energy's National Nuclear Security Administration under contract DE-AC04-94AL85000.

Issued by Sandia National Laboratories, operated for the United States Department of Energy by Sandia Corporation.

Available to DOE and DOE contractors from
U.S. Department of Energy
Office of Scientific and Technical Information
P.O. Box 62
Oak Ridge, TN 37831

Telephone: (865) 576-8401
Facsimile: (865) 576-5728
E-Mail: reports@adonis.osti.gov
Online ordering: http://www.osti.gov/bridge

Available to the public from
U.S. Department of Commerce
National Technical Information Service
5285 Port Royal Rd.
Springfield, VA 22161

Telephone: (800) 553-6847
Facsimile: (703) 605-6900
E-Mail: orders@ntis.fedworld.gov
Online order: http://www.ntis.gov/help/ordermethods.asp?loc=7-4-0#online

SAND2010-6310
Unlimited Release
Printed September 2010

Magnetically Applied Pressure-Shear: A new technique for direct strength measurement at high pressure

(final report for LDRD project 117856)

C. Scott Alexander, James R. Asay, Tom A. Haill, Derek C. Lamppa

Sandia National Laboratories
P.O. Box 5800
Albuquerque, New Mexico 87185

Abstract

A new experimental technique to measure material shear strength at high pressures has been developed for use on magneto-hydrodynamic (MHD) drive pulsed power platforms. By applying an external static magnetic field to the sample region, the MHD drive directly induces a shear stress wave in addition to the usual longitudinal stress wave. Strength is probed by passing this shear wave through a sample material where the transmissible shear stress is limited to the sample strength. The magnitude of the transmitted shear wave is measured via a transverse VISAR system from which the sample strength is determined.

ACKNOWLEDGEMENTS

Many outstanding individuals contributed to the success of this project. The authors wish to express our gratitude to the following people.

Ron Kaye and Tracy Vogler contributed early in this project through helpful technical discussions regarding magnetic field interactions and shear wave propagation respectively.

The experiments were conducted at the Sandia DICE facility where Randy Hickman and Jesse Lynch were responsible for operation of the MPG and Veloce. Sheri Payne was responsible for proper installation and fielding of the transverse VISAR diagnostics. Aaron Bowers assembled the shot hardware including the composite panels and the sample – anvil assembly.

Andy Shay designed and drafted much of the custom hardware required to implement an external magnetic field on Veloce. He and Jim Puissant also spent many hours in the winding shop fabricating the prototype magnet coils.

John Jojola and Gerard Torres assembled and tested the MPG hardware prior to delivery to DICE.

Early numeric simulation work on this project was completed by Greg Weirs and John Niederhaus.

Finally, management support for this project was consistent and greatly appreciated. Specifically, the willingness of Randy Summers, Dawn Flicker, and Ron Kaye to lend personnel to this project resulted in a diverse team. The support of Tom Mehlhorn helped launch this effort. Clint Hall and subsequently Mark Herrmann supported this effort by making the DICE facilities and personnel available. Mike Desjarlais and the entire SEE Investment Area Team provided generous funding which ultimately led to the successful development of an important new capability for Sandia.

Contents

FIGURES

TABLES

"If the truth be known, most successes are built on a multitude of failures."
-- Author unknown

1. INTRODUCTION

The strength of materials, defined as the ability of a material to sustain deviatoric (shear) stresses, at high pressures and strain rates is a critical aspect of material behavior for many applications including armor and weapons design and planetary science. It has proven extremely difficult to measure material strength under high-pressure dynamic loading because the governing equations for plane wave propagation provide no information about stresses in orthogonal directions.

Strength is an important aspect of the response of materials subjected to compression to high pressures. Beyond the elastic response, material strength will govern at what pressure and to what extent a material will plastically deform. After the equation of state, strength is perhaps the second most important material characteristic in the determination of the material state during and after compression. For this reason there is great interest within the Department of Energy (DOE) to accurately determine material strengths at high pressure. Within Campaign 2, this is currently the number two priority.

1.1. Existing strength measurement techniques

While many techniques exist to measure strength at modest pressures [1, 2, 3, 4], there are few applicable to the high pressure region of greatest interest to the DOE. One approach which has been used to determine the strength of aluminum to 160 GPa is the self-consistent technique [2]. This approach requires shocking a material to a high pressure state and then observing the material response while increasing and releasing the pressure via two separate experiments. This approach has been used for some time using gun driven plate impact experiments as it lends itself well to that geometry. Unfortunately, guns are limited in the pressures they can achieve and data is desired beyond that range. Pulsed power machines such as Z and laser facilities can achieve greater pressures but are not yet able to generate the reshock data that the self-consistent approach relies on. In addition, these methods require the use of optical diagnostic windows which limit the stress range to several Mbar pressures [5].

Pulsed power facilities, predominantly laser based, have turned to a second technique to attempt to measure material strength at greater pressure by exploiting the phenomena known as Rayleigh – Taylor (RT) instability growth [6, 7, 8]. By seeding a material interface with a sinusoidal perturbation, an RT instability is formed which will grow when exposed to a compressive wave. The growth of the instability is observed during the experiment and is later compared to a numerical simulation. Material strength is varied in the model in order to match the experimental result. While this approach is applicable to much higher pressures, it relies on a strength model to analyze the data and as such is dependent on the accuracy of the chosen model.

1.2. Existing strength models

Many models have been devised to represent material strength in hydrodynamic calculations. For the purposes of this report, several of the most common models will be briefly introduced. The purpose here is not to cover any of these models in detail but to provide an overview and references for the interested reader.

Strength models can generally be divided into two categories; physics based models which are built on the underlying dislocation dynamics and empirical models based on experimental results alone.

Among the more widely used physics based models are the Zerilli-Armstrong [9], Mechanical Threshold Stress (MTS) [10], and the Preston-Tonks-Wallace (PTW) [11] models. These models do not rely directly on experimental strength data to construct the model but rather use experimental data to validate the model predictions. Although this type of model may be more physically realistic, the strength predictions may not reflect reality in all cases. If the model has not considered an important physical mechanism for a particular problem, the strength predictions can be inaccurate.

Empirical models are based on the opposite approach. These models take experimental data, generally collected at a limited number of stress states, and use it to predict strength at intermediate states. Extrapolation of strength data can lead to wildly divergent predictions and so the models are generally only reliable aver the stress range of the data on which they are based. This caution has not prohibited extreme extrapolation out of necessity in general use as there are many stress ranges of interest over which there is limited experimental data.

The most widely used strength model for DOE applications is that of Steinberg and Guinan [12]. However, recent results have shown that this model may under predict material strength by up to a factor of two as a result of incorrect assumptions reducing the experimental strength values with which the model was calibrated [13]. A slightly more complex model proposed by Huang and Asay has been shown to more accurately predict strength [14]. Other empirical strength models include the Johnson-Cook model [15] which has advantages when applied to brittle materials such as ceramics.

1.3. Project goals

The goal of this project is to develop and demonstrate a new approach to measuring material strength using pulsed power MHD machines. The new approach, while being demonstrated at low stress levels using the Veloce small pulser, needs to be applicable on the Z machine which is capable of producing much greater stress levels. Further, it was desired that the method be independent of any strength models. That is, strength values should be determinable directly from the recorded data without the use of any numerical models or simulation of the experiment.

2. PRINCIPLE OF OPERATION

2.1. MHD drive

The use of electrical pulsed power to generate strong pressure waves in materials began around 1998 with the development of a technique utilizing the Sandia Z accelerator [16] to generate pressures approaching 1.5 Mbar (150 GPa) in aluminum [17, 18] via isentropic compression. The pressure drive was created by allowing a 90kV charge to flow through a ground short circuit resulting in a 22.3 MA current. This large current passes though parallel plate conductors, an inductive load, resulting in the generation of a large magnetic field between the plates. Interaction of the current and the self-generated magnetic field results in a Lorentz force and the

generation of a magnetic pressure wave. Since these early experiments, with refinements to the technique and upgrades to the machine, it is now possible to isentropically compress samples to pressures of 4 Mbar [19].

The Veloce small pulser [20, 21] operates on the same principle as the Z machine. It is a smaller device capable of producing 3MA currents resulting in magnetic pressures up to 20 GPa. This platform is an ideal test bed for new experimental approaches and diagnostics as it is much cheaper and easier to operate than Z. Figure 1 shows a cross sectional view of the load region in Veloce. During operation, the top panel initially sees the full machine charge (up to 70 kV) while the bottom panel is grounded. The resulting current, I, flows as indicated in the figure (represented by the current density, J) resulting in a self generated magnetic field, B, in the gap region between the panels. The subsequent J × B Lorentz force generates a magnetic pressure wave, P_{mag}, proportional to the square of the current (or B field), which acts to drive the panels apart. Pressure waves generated in this manner are generally referred to as a magneto-hydrodynamic (MHD) drive.

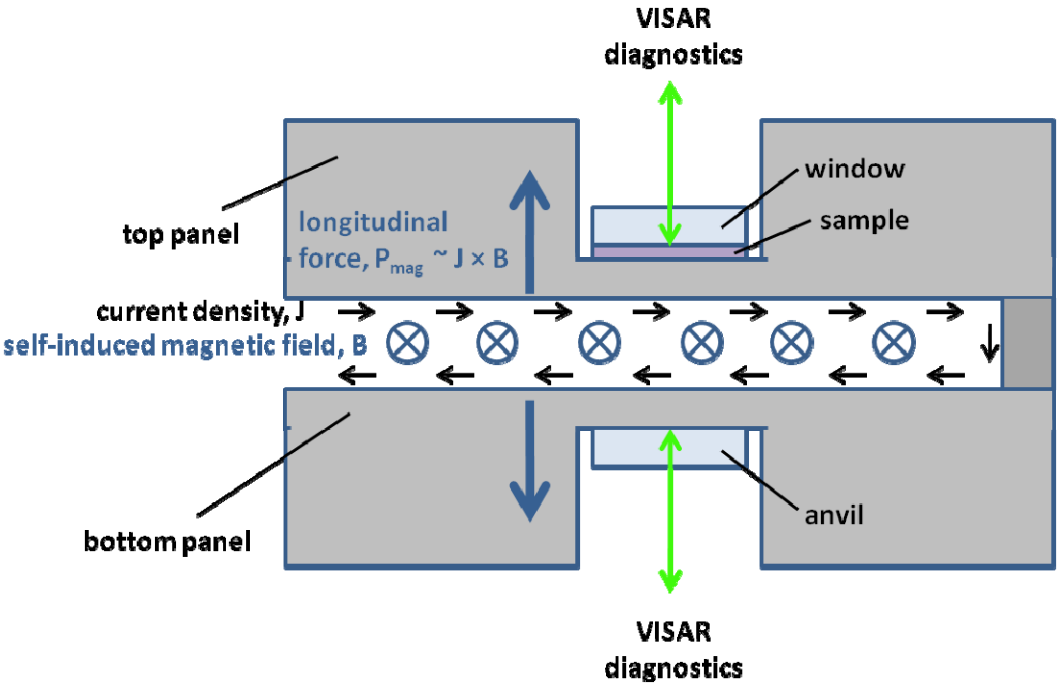

Figure 1: Cross sectional view of the load region of Veloce. Also shown is the typical sample configuration.

2.2. Addition of crossed B_o field

Consider the effect of an additional static magnet field, B_o, oriented such that the field is normal to the plane of the panels as shown in Figure 2. The MHD drive discussed previously will not be affected by this field as there will be no change in the current flow on the panels and, as a result, no change in the self-generated field in the gap. However, in addition to the J × B Lorentz force which produces P_{mag}, a second J × B_o Lorentz force will exist due to the interaction of the drive

current and the external field. This force will act in the plane of the panels, normal to the MHD drive as shown. Thus this force will directly induce in the panel a ramp wave with purely shear characteristics. With the additional B_o field in place, this configuration is referred to as magnetically applied pressure-shear or MAPS. A clever utilization of this technique is used to probe material strength under compression.

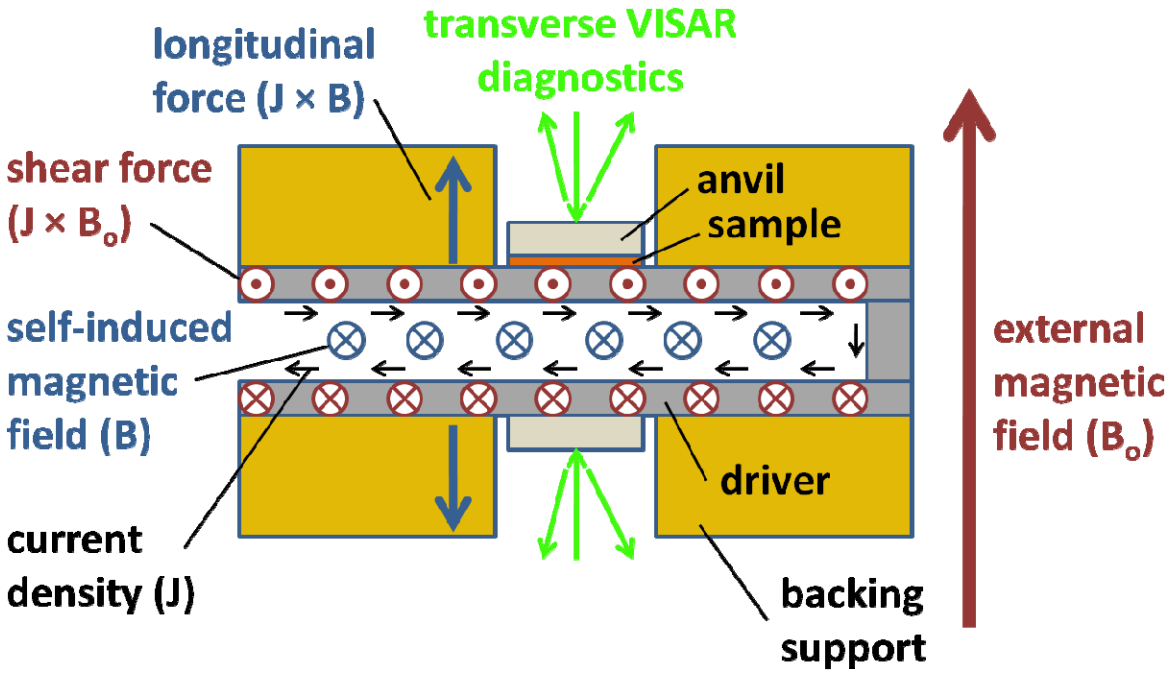

Figure 2: Cross sectional view of the Veloce load region configured for MAPS.

2.3. The principle of MAPS for strength determination

To determine strength, we exploit the property that, for a von Mises yield criterion, at a given longitudinal stress, σ, the maximum amplitude pure shear wave, τ, that can be transmitted through a material is limited by the strength at that stress level, $Y(\sigma)$, as $\tau \leq (1/\sqrt{3})\, Y(\sigma)$. This expression applies to pure shear stress only. A von Mises yield criterion leads to the more familiar relation $\tau_r \leq 2/3\, Y(\sigma)$ for resolved shear stress. The experimental configuration, shown in Figure 2, consists of one panel containing a high strength Mo driver, the test sample, and a high strength anvil. The opposing panel contains only the driver and anvil.

Upon transmission of the shear wave generated in the driver into the test material, only the shear stress equal to the critical shear strength of the test sample will be supported and ultimately transmitted into the anvil, which is elastic to the peak longitudinal stresses used and has higher strength than the test material. The longitudinal and transverse particle velocities are measured at the anvil free surface from which the test material compression and strength can be deduced.

The following sections detail several experimental design considerations that are critically important to the execution of these principles.

2.3.1. Wave speeds

Over time (on the scale of ns), both the current, which is initially on the surface of the panel, and the self-induced magnetic field, initially internal to the gap, will diffuse into the panel material based on rate equations dependant on the panel material properties. The diffusion of these previously external fields results in changes in the material state. This is particularly evident as the drive current permeates the panel where Joule heating results in melting or conversion to plasma. As the panel melts and/or ablates, it will lose strength and will have changes in the electrical properties effecting later diffusion rates through the region. The boundary between the undisturbed region and that where the drive current or field has diffused into the panel is referred to as the diffusion front and can be thought of similarly to a propagating wave front.

It is critically important that the pressure waves generated during the MHD drive outrun the diffusion front thus preventing influence of the physical changes in the panel material. It has been previously shown that this condition is satisfied for the longitudinal wave [18, 22]. Shear waves travel slower than longitudinal waves. If the shear wave generated does not outrun the diffusion front, it cannot be used to probe the sample strength. Numeric simulations (detailed in the following section) verified that the shear wave would propagate faster than the diffusion front. Thus, wave evolution is such that the longitudinal compression wave travels faster than the shear wave resulting in materials being compressed prior to application of shear which occurs prior to the arrival of the diffusion front. This condition is illustrated in Figure 3.

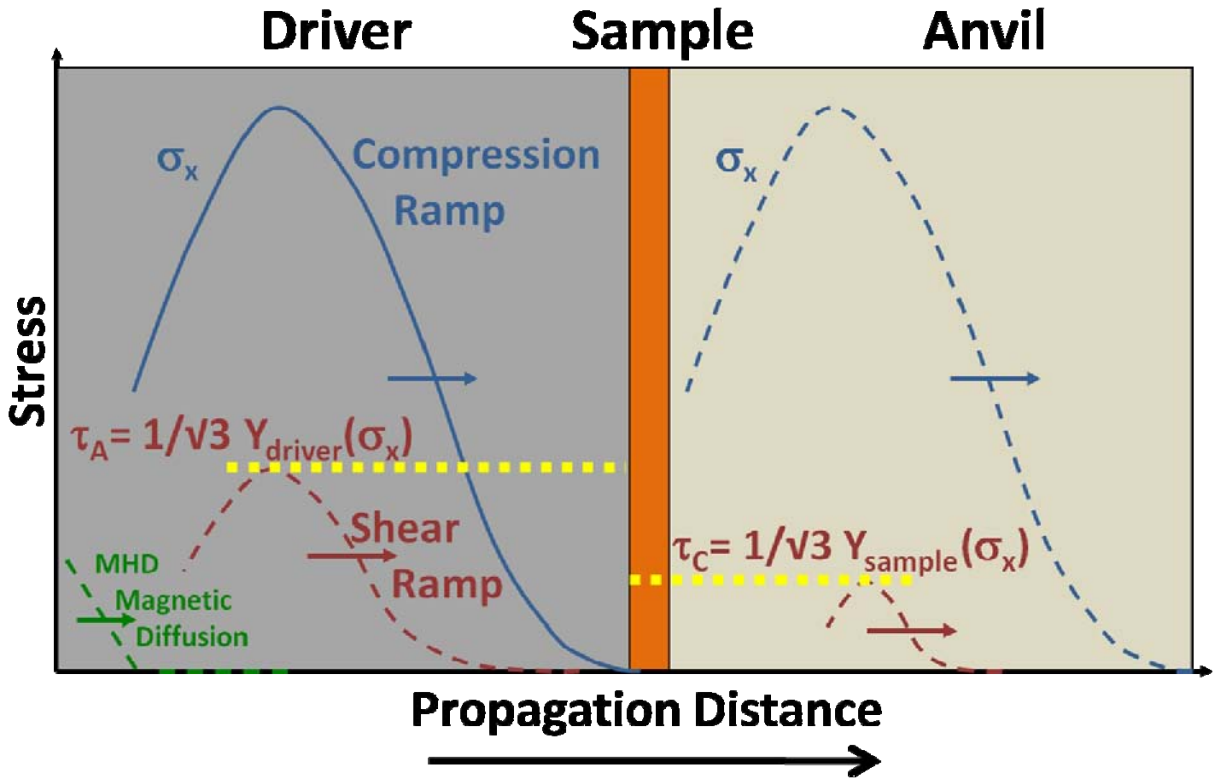

Figure 3: Wave propagation during a MAPS experiment.

2.3.2. Requirements for driver and anvil materials

Several conditions restrict the choice of driver and anvil materials. The driver material must be electrically conductive to allow for an MHD drive. However, the magnetic permeability of a material is inversely proportional to the electrical conductivity. The external magnetic field must permeate the driver quickly enough to allow for static conditions prior to the MHD drive. Thus there is a balance that must be considered. Fortunately, due to the limited thickness of the driver, even for relatively good conductors (e.g. aluminum) the external field will permeate the panel.

In order to probe the sample strength, the shear wave generated in the driver must be of greater magnitude than the shear strength of the sample in order to reach the yield surface in the sample. The maximum shear that can be generated in the driver is limited by the driver shear strength. Thus, the driver must have greater (or equal) strength than then sample.

The strength of the anvil is also important. The anvil must be able to support the entire shear transmitted from the sample to prevent further truncation of the shear wave magnitude and provide an accurate measure of the sample strength. Thus the anvil must also be stronger than the sample. There is no requirement that the anvil be electrically conductive. In fact, it is preferable to have a non-conductive anvil material to enhance the magnetic permeability.

2.3.3. Stress coupling

For inelastic materials, assuming elastic-perfectly plastic response and a von Mises yield criterion, the longitudinal and shear stress deviators are coupled through the yield function [23]

$$\frac{1}{3}Y_o^2 = \frac{3}{4}S_{xx}^2 + S_{xy}^2 \quad (1)$$

where Y_o is the yield strength, S_{xx} is the longitudinal stress deviator commonly referred to as the resolved shear stress, and S_{xy} is the shear stress deviator also known as the applied pure shear stress. These quantities are plotted in Figure 4 for a simulation of the experimental configuration.

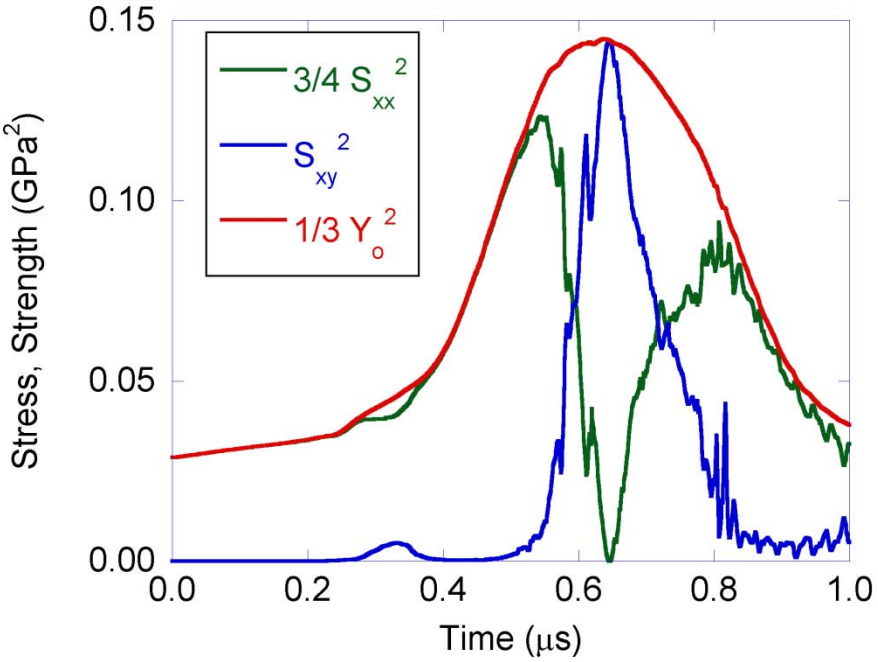

Figure 4: Simulation results showing resolved (S_{xx}) and pure (S_{xy}) shear stresses and yield strength (Y_o) in the sample.

A longitudinal wave propagating in an inelastic material will induce shear stress components governed by equation (1) as a consequence of the coupling of the shear components. The use of an inelastic driver material in these experiments resulted in generation of a small coupled shear response observed in Figure 4as a "precursor" shear wave which peaks in the sample at about 0.3 μs, the time of the elastic to plastic transition in the longitudinal wave. This coupled shear wave is transmitted through the sample and is combined with the longitudinal deviator to satisfy equation (1) during yielding in the plastic portion of the longitudinal wave. A similar effect in the anvil is avoided by the use of an elastic anvil material.

2.3.4. Design considerations

The relative thicknesses of the driver, sample, and anvil must be carefully considered. Strength must be probed in the sample at peak compression and due to the difference in longitudinal and shear wave velocities, the driver must not be too thick to allow separation of the waves beyond a tolerance set by the shape of the MHD drive current pulse which determines the width of the longitudinal compression peak. To this same end, the sample must be thin enough that the required reverberation of the longitudinal compression occurs quickly. This will provide a uniformly compressed state in the sample at the time strength is probed. The anvil thickness will control the degree of interaction between the reflected longitudinal wave and the forward propagating shear wave. It must be thick enough to prevent the reflected longitudinal wave from reaching the sample, and releasing the stress, prior to the passage of the shear wave. Conversely, the anvil must be thin enough to allow the shear wave to reach the free surface and be detected prior to any edge effects.

Figure 4 shows that the strength of the sample is probed at the maximum value corresponding to peak longitudinal compression as the yield strength is modeled by the Steinberg-Guinan model

[12] and is proportional to pressure. The pure shear wave (S_{xy}) passes through the sample at about 0.65 μs. This results in a reduction in the resolved shear stress (S_{xx}) to zero. In this state, the pure shear stress equals the yield strength in accordance with equation (1). Thus, the shear stress deviator is a valid measure of yield strength. The requirements for continuity of stress and particle velocity across boundaries in the absence of slippage indicate that this shear stress will be transmitted into the anvil which is elastic and of higher yield strength.

3. NUMERICAL SIMULATIONS

Numeric simulation was used heavily in the design phase of this project. Initially, simulations demonstrated the feasibility of the MAPS concept and later provided an important view of the internal state of the materials. Such insight was invaluable in understanding the complex interactions between the coupled applied and resolved shear stresses and the effects of material interfaces and wave interactions. Finally, optimization routines were used to determine the best thicknesses for the individual materials in the experimental configuration. The following sections describe the models used and summarize the key results.

3.1. Description of the ALEGRA MHD Analysis Code

The ALEGRA-MHD simulation code [24] models geometrical domains that may be two-dimensional (Cartesian (XY) or cylindrical (RZ)) or three-dimensional (Cartesian (XYZ) only). The meshes are unstructured and finite-element based and may be Lagrangian, Eulerian, or ALE (arbitrary-Lagrangian-Eulerian). The code is written predominantly in the C++ programming language which enables an object-oriented approach to implementing the physics algorithms. The code is massively parallel and runs on a large variety of computing platforms.

Object oriented programming allows the coupled physics to be readily operator split. The coupled physics includes solid dynamics, transient magnetics, thermal conduction, and radiation transport (if necessary). Radiation transport is not used for these simulations. The solid dynamics algorithm employs analytic and tabular equations of state, and constitutive models for the elastic-plastic deformation of materials. The strength model tracks the phase (solid, liquid, etc.) of the material and turns off the strength model when melting is detected, usually when the material state exceeds the Lindemann melt curve. The transient magnetics algorithm utilizes the MHD approximation, specifically that materials are charge neutral, so that the displacement current term in Ampere's Law is neglected, and the current density is divergence free. The MHD equations are closed using a basic form of Ohm's Law.

ALEGRA-MHD has been used over many years to model a variety of applications that are of direct relevance to shock compression and ramp loading of materials. The code has modeled magnetically accelerated flyer plates for nearly a decade. Early experiments launched metal flyer plates, such as Ti, Al, and Cu, to velocities on the order of 10~km/s. A concerted modeling effort elucidated the detailed physics of flyer launch enabling aluminum flyers to be accelerated to speeds of 20~km/s. Modeling helped to confirm Hugoniot measurements on aluminum in the stress range of 100- 500~GPa. The measurements were compared to model results for a variety of aluminum equations of state (EOS). Further optimization using MHD simulations to shape the current pulse eventually allowed the shockless acceleration of aluminum flyer plates to 30-34~km/s.

Current pulse shaping and shockless flyer plate acceleration enable another category of experiments known as isentropic compression experiments (ICE). ICE experiments can provide data to be measured along an entire EOS isentrope simultaneously. This allows the mapping of equation of states along the isentrope, which is in addition to the Hugoniot measurements generated by the flyer plate technique. MHD simulations are used routinely to model and design ICE experiments.

ALEGRA-MHD has been used for system studies of the Veloce pulsed power machine. Veloce is well suited for studying ICE. Not only has the acceleration of flyer plates been studied, but ALEGRA-MHD was extensively used to model the uniformity of current flow through the machine and into the load, as well as the uniformity of the magnetic pressure drive of the stripline panels that house the flyers. Experiments conducted on a similar pulser located at Washington State University to study the fragmentation of magnetically accelerated flyer plates were also modeled with ALEGRA-MHD.

Finally, EOS and electrical conductivity models are critical to high-fidelity simulations. Subtle differences between experiment and simulation led to efforts to improve these models. Revised parameter fits to experimental data soon gave way to detailed *ab initio* quantum molecular dynamics (QMD) simulations based upon density functional theory. The EOS and conductivity models used by ALEGRA-MHD are constantly being revised and improved due to these efforts.

3.2. ALEGRA modeling of MAPS experiments

The MAPS experiments were modeled using the ALEGRA-MHD simulation code. The simulations assume sufficient uniformity near the center of the experimental sample to take advantage of translational uniformity. The simulations use a 2D Cartesian mesh, even though the simulations are essentially 1D, i.e., all quantities are functions of the x-position and time only. The simulation domain is illustrated in Figure 5. The mesh is periodic in the y-direction. Periodicity enables a reduced simulation size, but still allows for shear motion in the y-direction. Longitudinal motion occurs in the x-direction and transverse motion in the y-direction.

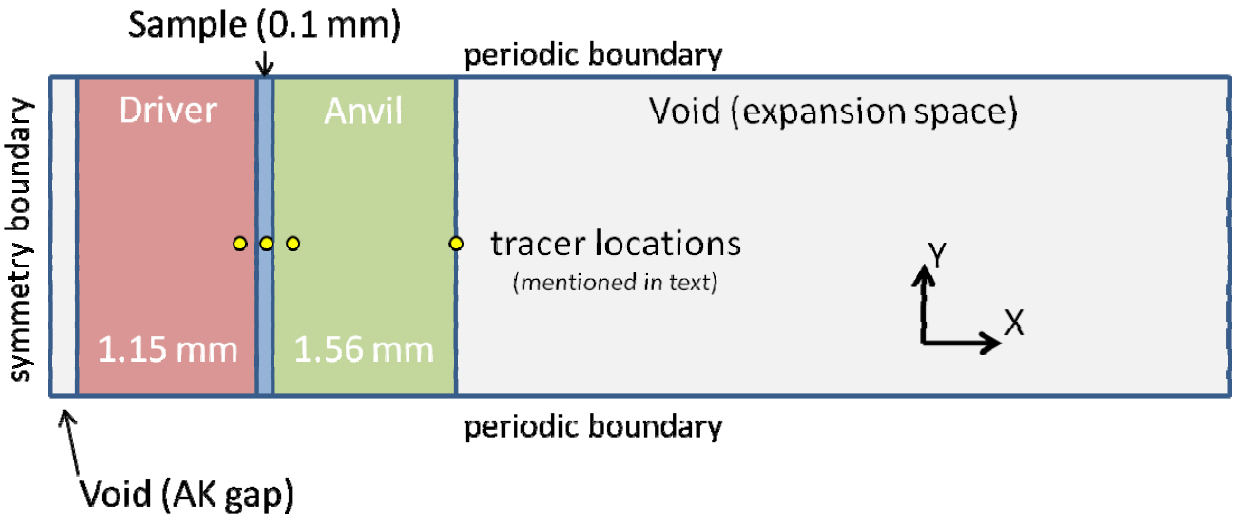

Figure 5: Illustration of the computational domain used.

The composite panel has its materials layered in the longitudinal (x) direction. To simulate the MHD drive, a time-dependent magnetic field, *B* (discussed previously in section 2.1) oriented in the negative y-direction, is applied at the left-hand boundary at x=0, according to

$$B(t) = f(t)\,\frac{\mu_o I(t)}{W+G} \tag{2}$$

Where *I(t)* is a standardized characteristic current profile typical of Veloce performance, the denominator, W+G, is a characteristic length defined by the sum of the panel width and inter-panel gap, and *f(t)* is a scale factor that accounts for 3-dimensional effects. While the scale factor *f(t)* is in actuality a time-dependent factor due to panel separation and deformation, as well as magnetic field diffusion, in practice an average constant value is employed. A zero y-component of the magnetic field is applied at the right-hand boundary. The curl of this field yields the current density, J, which flows in the z-direction perpendicular to the mesh. The Lorentz force (J×B) between this field and the current density accelerates the panel in the longitudinal direction. Joule heating melts and vaporizes the driver layer of the panel. This field is diffused through the panel according to the local value of the electrical conductivity. A static, uniform magnetic field, B_o, is applied in longitudinal direction. The Lorentz force between the longitudinal field and the current density ($J \times B_o$) generates shear forces and deformation in the panel. The longitudinal stress wave outruns the shear stress wave, which in turn outruns the magnetic field diffusion resulting in material generated waves which are undisturbed by the diffusion of the magnetic field and the associated ablation of the material.

The molybdenum driver layer is modeled using a Sesame tabular equation of state [25], the Steinberg-Guinan elastic-plastic strength model [26], and the Lee-More-Desjarlais electrical/thermal conductivity model [27, 28]. The aluminum sample layer is modeled in a similar manner [29]. The zirconia anvil layer is modeled using a Mie-Gruneisen equation of state [25], a highly-elastic perfectly-plastic strength model, and constant low electrical/thermal conductivity model.

Table of Model Parameters			
Material	Equation of State	Strength Model	Conductivity Models
Molybdenum	KEOS Sesame ANEOS 2984	CTH Elastic Plastic w/ Steinberg-Guinan	Lee-More-Desjarlais (LMD)
Aluminum	SNL Sesame 3720	CTH Elastic Plastic w/ Steinberg-Guinan	Lee-More-Desjarlais (LMD)
Zirconia	Mie-Gruneisen Us-Up EOS	CTH Elastic w/ High Yield Strength	Constant Electrical / Thermal Conductivity

Table 1: Models used in ALEGRA simulations of MAPS experiments.

3.3. Results of simulations

In order to illustrate the typical simulation results, we consider a simulation of what was ultimately the experimental configuration used for MS-10. The input deck used is shown in Appendix A. Simulation results were generally considered by observation of the response at five selected tracer points, shown in Figure 5. These critical points detail the response in the driver, sample and anvil as well as at the free surface and the sample anvil interface (noted as al-zr in the figures).

Particle velocities at the tracer locations are shown in Figure 6 and Figure 7 for v_x and v_y respectively. Particle velocity at the anvil free surface is the experimentally measured quantity and so is of particular interest in these results. In the actual MAPS experiments, experimental pressure and shear values will be determined from these quantities. For the results shown, the peak longitudinal and transverse free surface velocities are 480 m/s and 22.7 m/s respectively. *In-situ* values will be half as much. These values are determined at the second peak shown. The initial peak (much lower magnitudes) is a result of the stress coupling and associated with the yielding of the driver material. This effect will be discussed further below.

In order to calculate stress levels, the initial anvil density (known from the code input to be 6.028 g/cm^3) and the longitudinal and shear wave speeds (in the anvil) are required. For details, see section 5.1 below. The ability of the code results to be extracted from internal tracer points makes these quantities easy to determine. By observing the time shift between the curves at the aluminum-zirconia interface and the free surface the longitudinal and shear wave speeds are found to be 7.99 km/s and 5.56 km/s respectively. Combining these results gives peak pressure and shear stresses of 11.56 and 0.38 GPa.

The effects of melting and ablation of the driver material can also be seen in Figure 6 and Figure 7. At about 0.8 μs, fluctuations are apparent in the longitudinal velocity and the transverse velocity begins to increase considerably. This is due to the loss of strength and consequent unimpeded flow in the driver material. This does not affect the MAPS results as the compressing longitudinal and probing shear waves have already been generated and propagated out of the material before it is melted or ablated.

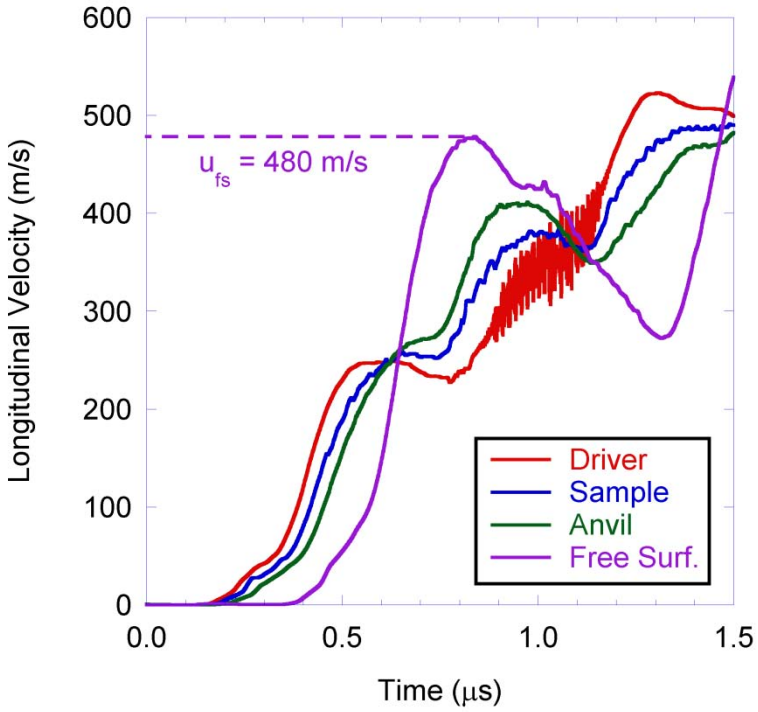

Figure 6: Simulated longitudinal particle velocity.

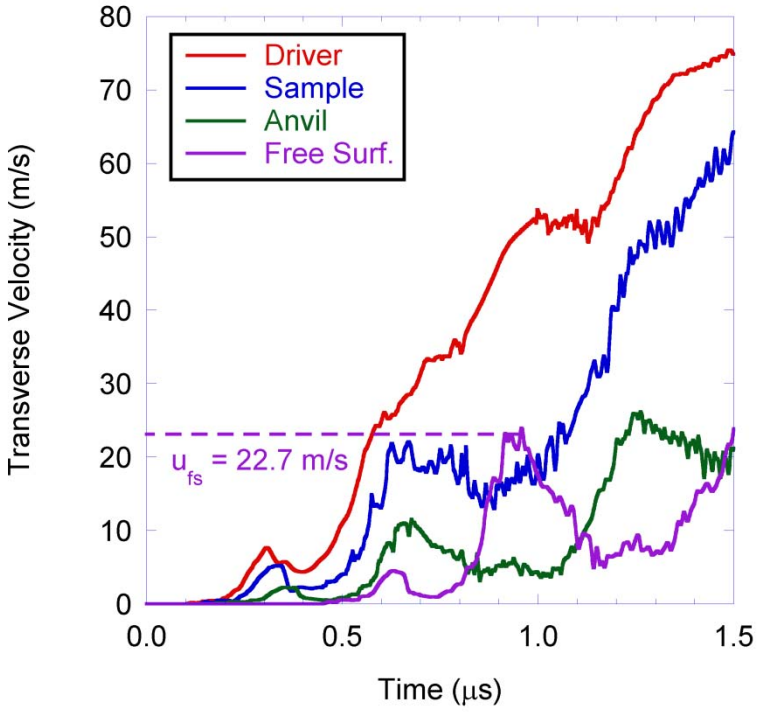

Figure 7: Simulated transverse particle velocity.

Tracer longitudinal and shear stresses are plotted in Figure 8 and Figure 9 respectively. The analytic stress values determined from the free surface velocities given above are also shown as dotted lines. It is clear that the analytic principles behind the determination of peak stress levels based on peak recorded velocity levels are sound. The agreement between code calculated longitudinal and shear stresses in the sample and the values inferred from analytic analysis of the code generated free surface velocities is nearly perfect, with any small deviation the result of numeric effects such as rounding in the code. Also of note in Figure 9 are the relative shear stress levels in each material. The greatest shear stress is in the driver where it is limited only by the inputs (B_o and I(t)) and the shear strength of molybdenum, modulated by the effects of Joule heating.

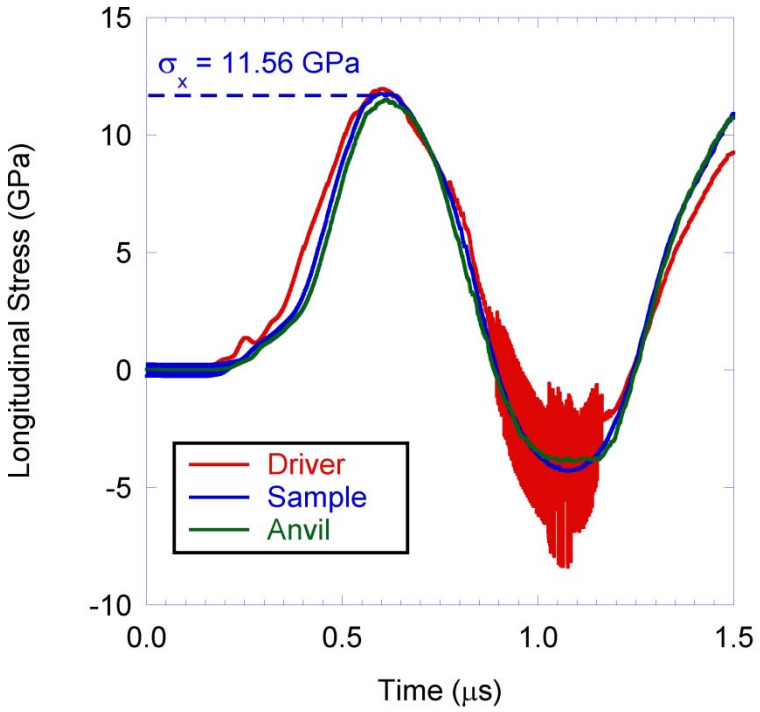

Figure 8: Simulated longitudinal stress.

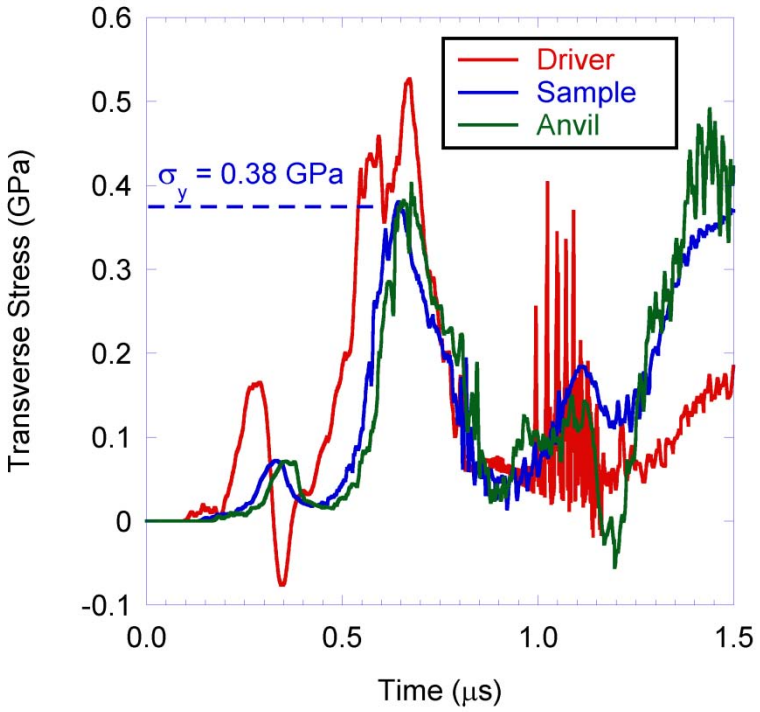

Figure 9: Simulated transverse stress.

Although not apparent from these plots, it is noted that the wave velocities determined by ALEGRA are larger than those measure experimentally (see section 5.3 below). This discrepancy has little effect on the interpretation of the results as the simulation is entirely self-consistent. The problem is believed to originate in the EOS model used for zirconia. Work is in progress to correct the model to provide better results in the future. The MAPS data described below will play an instrumental role in correcting and validating the zirconia model. This capability is a symbiotic result of this project.

The analytic results proved extremely useful in understanding the complex stress coupling described by equation 1 above. Figures 10, 11, and 12 below show the quantities of equation 1 evaluated at the tracers in the driver, sample, and anvil respectively. In all cases we note that the equality holds and the sum of the left hand side components equals the right hand side as indicated by the overlap in the figures. Considering each material individually provides insight into both the generation and propagation of stress waves during the experiment.

Figure 10 shows the coupling plot for the molybdenum driver. Initially, there is no applied stress (S_{xy}) at this location and the resolved stress (S_{xx}) increases with pressure as the longitudinal wave passes. The driver material yields at the point where this curve intersect the strength curve indicating the equality of equation 1 now holds. At this point, near 0.25 μs, a small deviation is observed in S_{xy} as a result of the yielding of the material. This small magnitude applied shear wave propagates through the remaining materials unchanged as the magnitude is less than the elastic limit in any of the materials. It is observed as the first small peak in the free surface particle velocity. As it does not result in yielding of any materials, this shear wave is of no

consequence to the end results. Following the yield, the drive pressure increases to a maximum value determined by the input current. Near, but slightly before, the peak compression, the applied shear wave resulting from the interaction of the drive current and the external field arrives at the tracer location. This increase in S_{xy} requires a decrease in S_{xx} as dictated by the equality in equation 1.

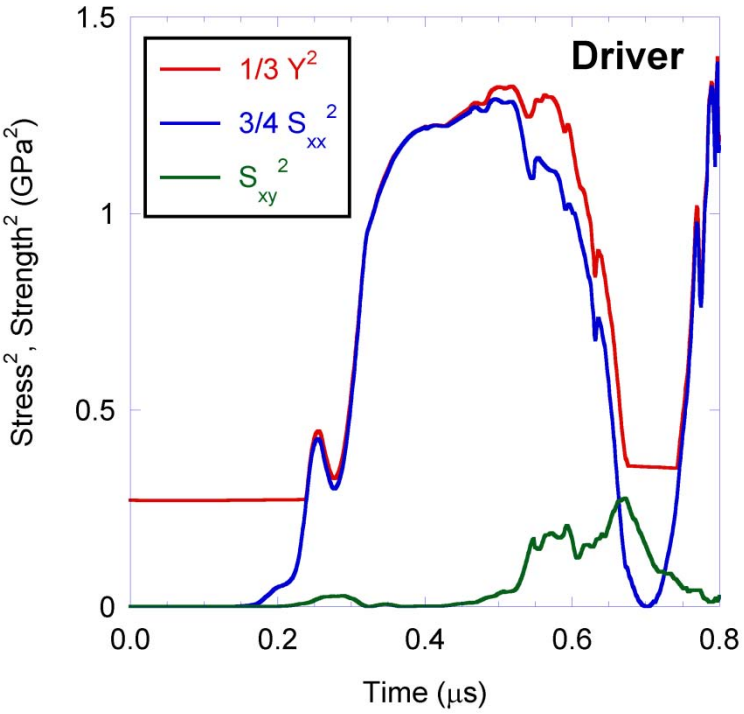

Figure 10: Stress coupling plot for the driver.

Figure 11 shows a similar relation for the tracer point in the sample. Here, the longitudinal compression is easily observed as an increase in the yield strength. Again, S_{xy} is initially zero as the applied shear wave has not reached the sample. The arrival of the small precursor wave is seen at about 0.3 μs and a corresponding drop in S_{xx} is observed. The arrival of the applied shear wave is seen at about 0.5 μs with a peak at about 0.65 μs. Again, this results in a reduction in S_{xx} based on the equality in equation 1. Unlike for the precursor wave, in this case the applied shear is sufficient to bring the material to the yield surface and drive S_{xx} to zero. This is critical for the observed shear wave in the anvil to accurately convey information on the strength of the sample. Also important is that the applied shear wave passes through the sample at the peak longitudinal compression. The sample thickness is limited to ensure that this holds to within 1%. The shear wave is about 1/3 the width of the longitudinal wave allowing for a finite amount of time for the shear wave to transit the sample while within 1% of the peak compression. If this condition is violated, the measure strength will be less than that at peak compression as the applied shear will be limited by the strength at a lower compression. In the future, it may be possible to widen the input current pulse, which will increase the width of peak shear compression and make analysis of the shear free surface particle velocity more reliable.

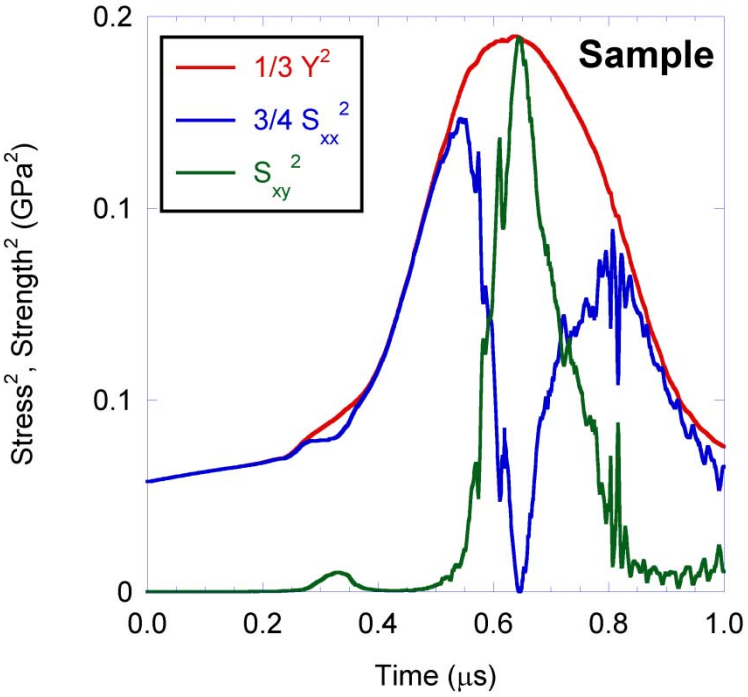

Figure 11: Stress coupling plot for the sample.

Figure 12 shows the coupling plot for the anvil. Here, the transmitted applied shear from the sample is small compared to the yield strength of zirconia. The peak value of S_{xy}^2 is about 0.16 GPa^2. Clearly, the condition that the anvil be strong enough to support the transmitted sample shear is met in this case.

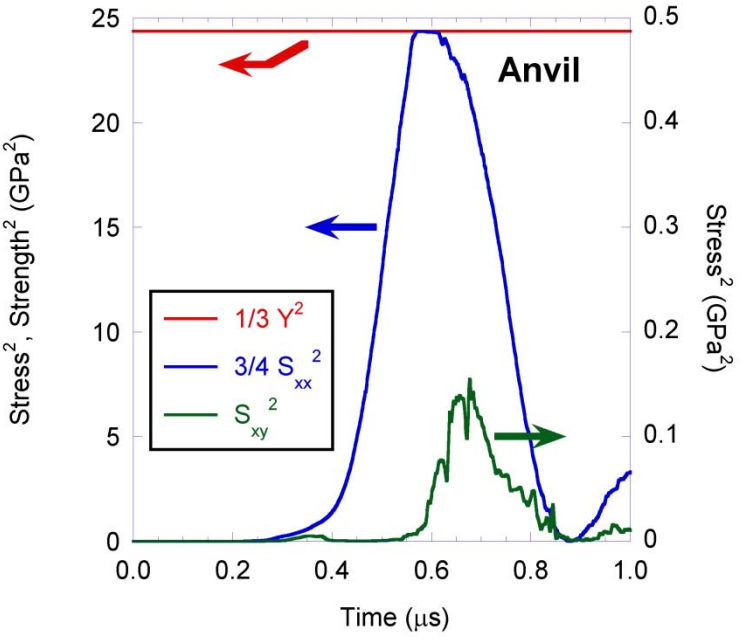

Figure 12: Stress coupling plot for the anvil.

4. EXPERIMENTAL APPARATUS

4.1. Veloce small pulser

The operation of the Veloce small pulser, shown in Figure 13, has been described in detail elsewhere [20, 22]. For the purposes of this report, we consider only those elements of operation that are directly relevant to the design of the MAPS technique.

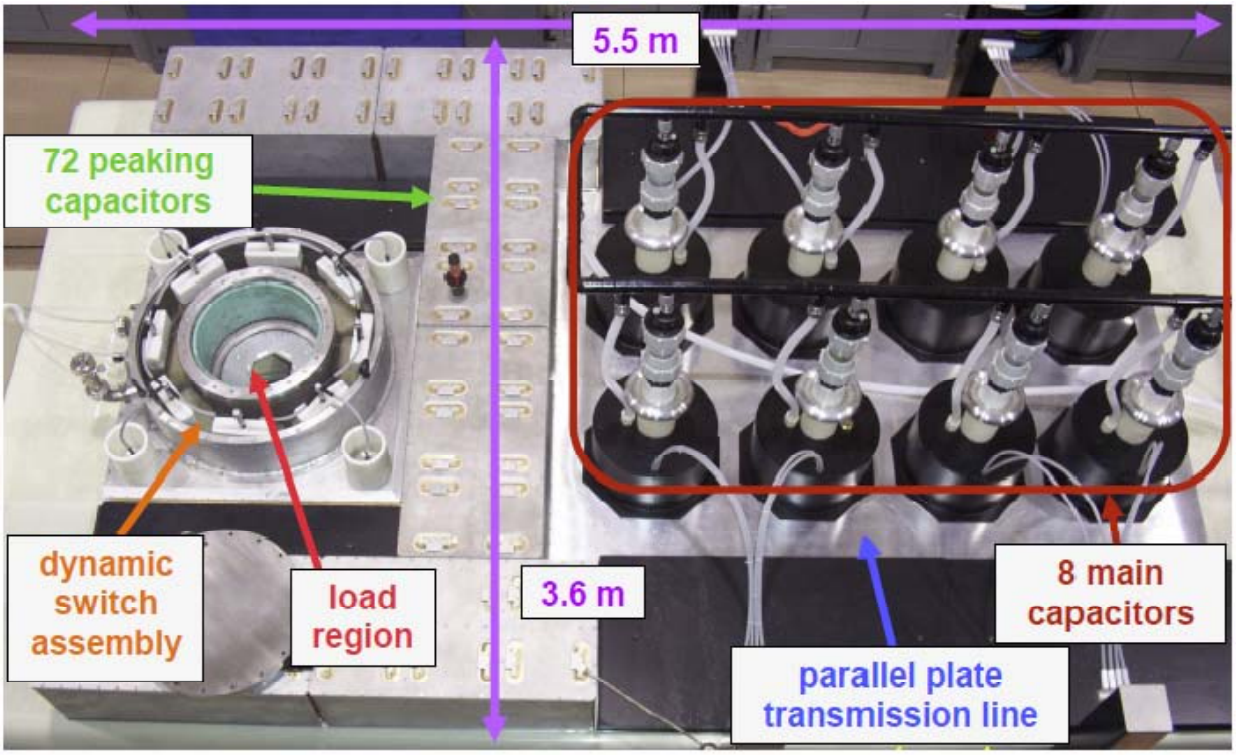

Figure 13: The Veloce small pulser. Taken from figure 3.1 in reference [20].

4.1.1. Integration of an external magnetic field

In order to apply the external magnetic field required for MAPS, a set of coils needed to be installed in close proximity to the sample region without restricting diagnostic access. The greatest limitation on the design was space. The tank (cylinder inside the dynamic switch) shown on the left of Figure 13, surrounds the load and provides containment of shot debris. The magnet coils were required to fit inside the tank and were also limited in size by the presence of a clamping bar. A close-up view of the tank is shown in Figure 14. The magnet coils were required to be coaxial with the panel counterbore (under the VISAR probes in the figure) which fixed the location of the coil center. The clamping bar limited the maximum diameter of the coils to 4.5 inches. Thus, a set of magnet coils capable of producing a uniform 10T field at the sample subject to these space constraints were required. The development of these coils is described in detail in the following section.

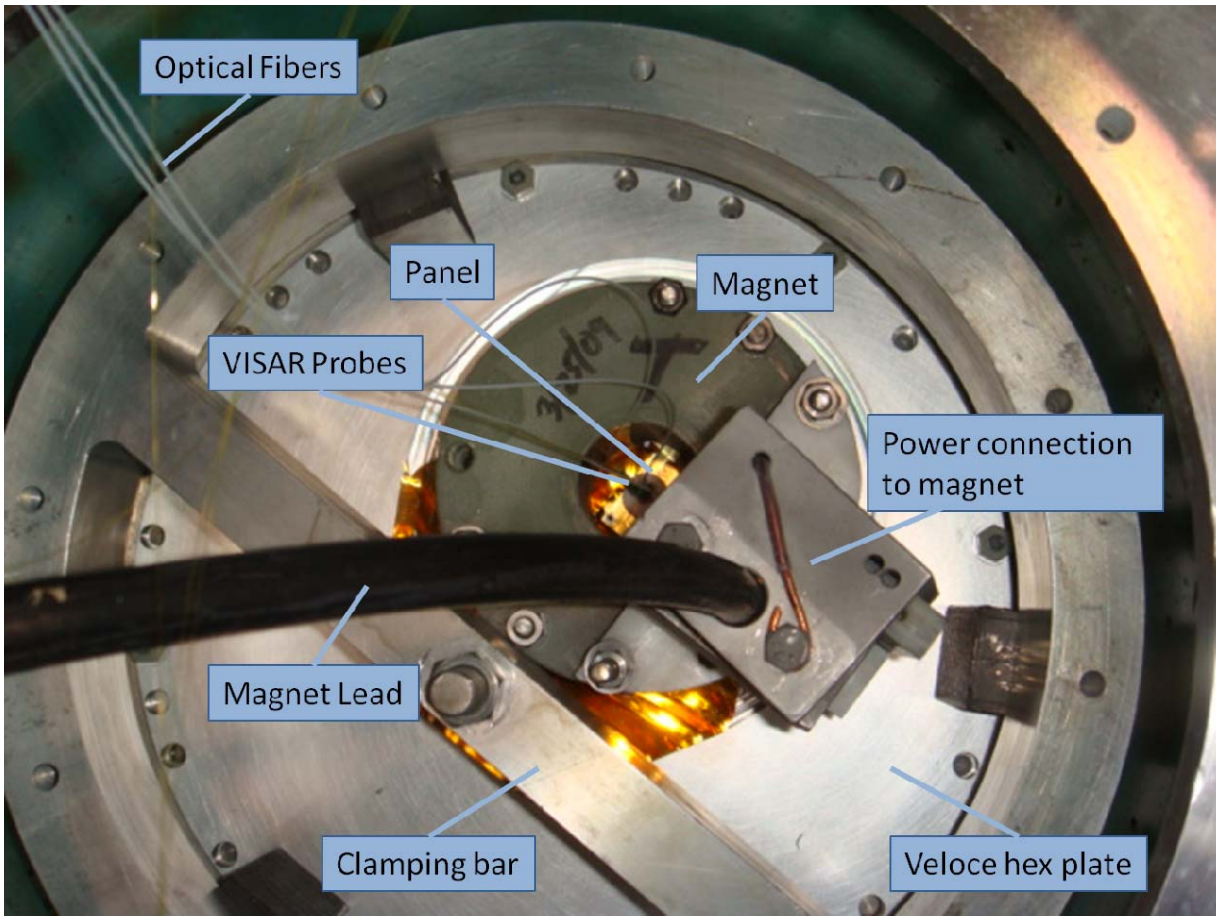

Figure 14: View of the Veloce tank with a MAPS experiment installed.

4.1.2. Mo/brass panels

The Veloce panel design also required modification for MAPS. In a normal configuration, the panels are made of a single piece of either copper or aluminum. Neither of these materials has sufficient strength to support a large enough shear drive. The selected driver material, molybdenum, is strong enough but as such is also difficult to machine. The process of counterboring a solid molybdenum panel would be time and cost prohibitive. The solution was to construct a two-part panel with the power flow region separate from the bulky support region surrounding the counterbore. This design is shown in Figure 15. The gray material is molybdenum while the golden backing material is brass. One concern with a two part panel design was that power might flow not on the bottom surface but also on the top of the molybdenum layer. If the backing material has a higher electrical conductivity than molybdenum, it is likely that a significant fraction of the power flow would be on the backing (or the top of the driver). This was avoided by selecting brass for the backing material. Brass is not only cheap and easy to machine, it also has a lower electrical conductivity than molybdenum (15.9 MSiemens/m vs. 18.7 for Mo). By restricting the difficult to machine molybdenum to the critical drive region and constructing the backing support out of softer brass costs were kept down without sacrificing machine performance.

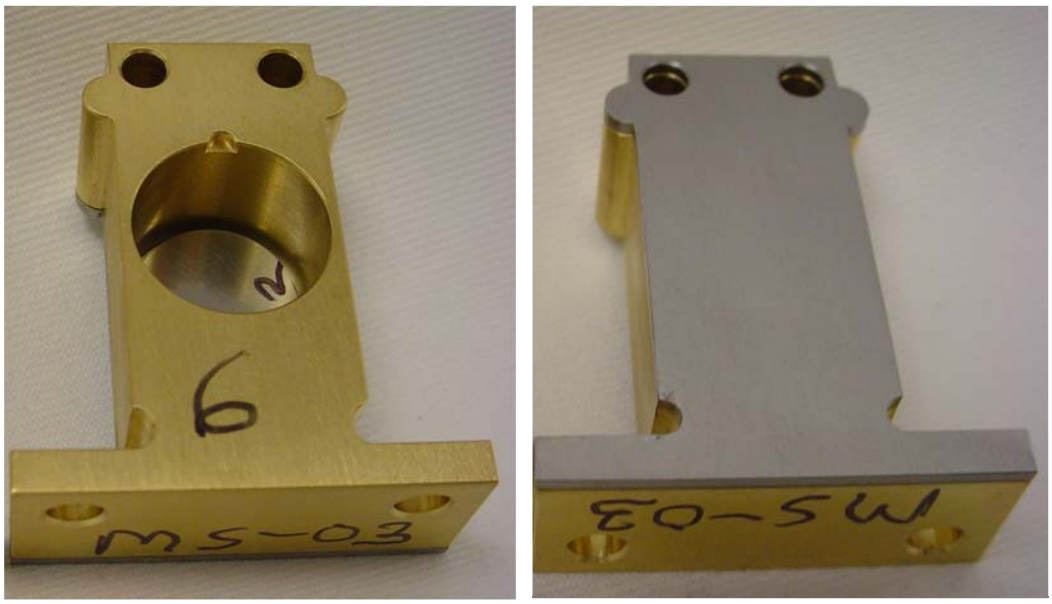

Figure 15: A composite molybdenum/brass panel.

4.2. Magnetic Pulse Generator

To enable this novel approach to measuring material strength, a low-frequency magnetic field source was needed to premagnetize the sample. Department 5445 was approached to develop a capacitor bank system that could energize a pair of field coils mounted around the sample in the VELOCE tank. This coil pair is designed to provide uniform magnetic field normal to the face of the sample. The following figure provides a notional cross-section located on either side of the test sample on the VELOCE plates. The composite housing of the windings are seen in green and red, with the copper conductors shown as discrete hoops. Also shown is the composite overwrap (in yellow) that prevents radial expansion of the coil windings during the current pulse.

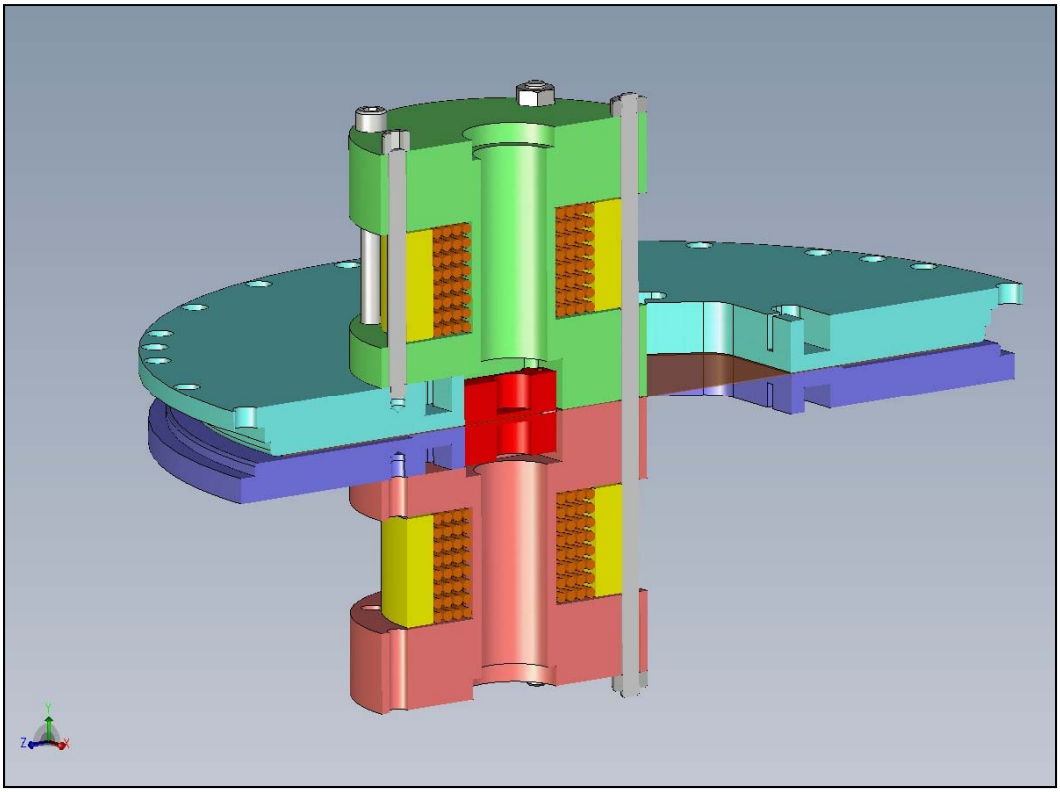

Figure 16: Notional cross section of coil pair on VELOCE hardware

The capacitor bank designed for this effort, known as the Magnetic Pulse Generator (MPG), was required to meet the following design criteria:

- Must be able to achieve 10T at test sample
- Must provide ~1% uniformity across sample 7mm radius
- Slow magnetic time variance compared to the VELOCE coil pulse
- Coil pair must fit within existing hardware and accommodate experiment instrumentation
- Coils must be symmetric around the panel feeds
- System performance must be repeatable shot-to-shot

4.2.1. The MPG Pulsed Power Circuit

The capacitor bank circuit and the coils are closely coupled design efforts but are discussed separately here.

MPG Capacitor Bank

The drive circuit developed for this application is a parallel capacitor bank isolated from the coil load by a bi-directional control thyristor switch. The four 2.25mF capacitors, charged to a user-specified voltage by a TDK-Lambda Constant Current Supply (CCS) power supply, are

discharged into the inductive load following a command pulse from the controller that closes the main thyristor switch. The current pulse rises through the coils, with the entire bank behaving as an under-damped RLC circuit. Just after time of peak current, when the voltage is beginning to reverse on the capacitor bank, a second command pulse closes the Crowbar Thyristor.

The crowbar leg of the circuit provides a low-impedance path (R= 80mΩ with negligible inductance) for the coil current to flow without charging the capacitors in reverse polarity. This reduces the impact on capacitor lifetime with the 2.25mF capacitor banks. When charged to the power supply's maximum output voltage, the MPG system provides 110kJ of electrically stored energy. An early simulation of the capacitor bank circuit follows in Figure 17. A nominal coil impedance is included at the end of the transmission lines of R = 119mΩ and L = 603μH.

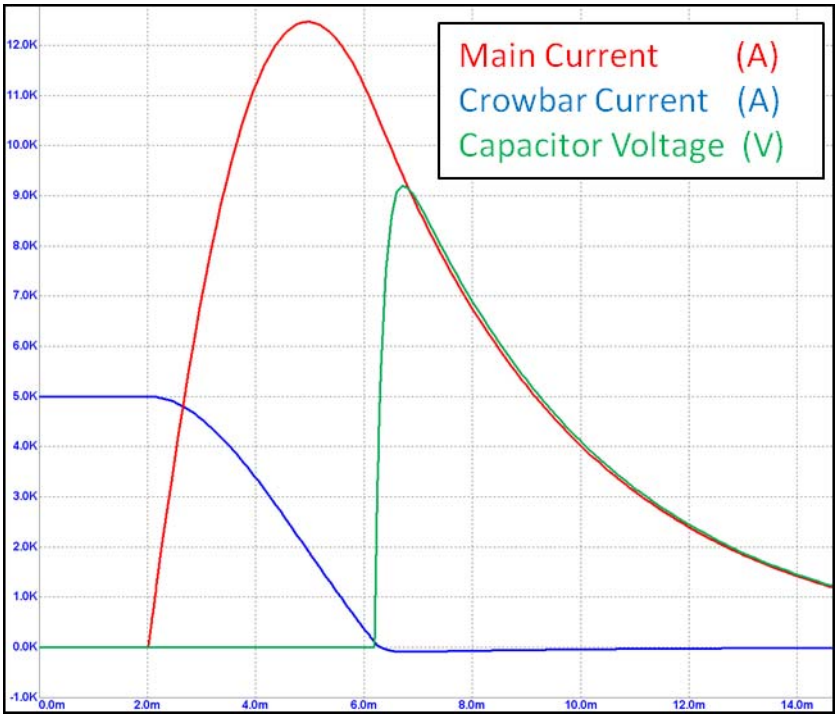

Figure 17: MPG simulated transient behavior versus time (ms)

Figure 18 shows the Microcap® circuit simulation used to generate these results. Linking the capacitor bank is the circuit equivalent of two parallel 20ft transmission lines. This circuit represented the point design that was the start for MPG. The evolution from this point design will be detailed in a later section.

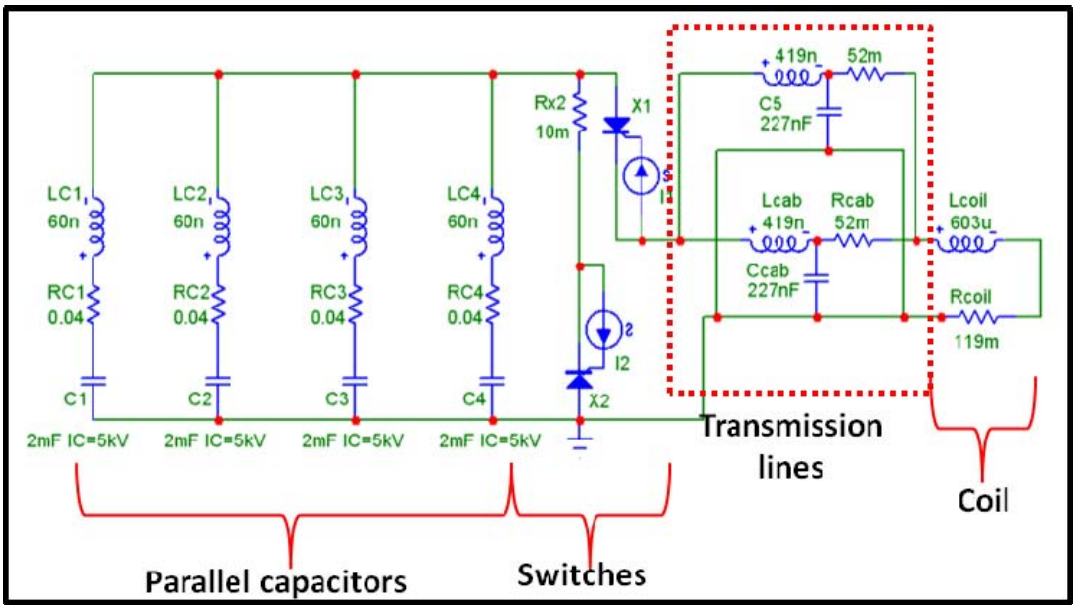

Figure 18: Microcap schematic for MPG circuit design

The General Atomics 2.25mF capacitors were rated to 5kV. A compressed thyristor switch stack containing the two thyristors and associated snubber circuitry was converted from another experiment to support the MPG application.

Coil Design

The design of the coil pair required balancing the geometry requirements (space constraint and probe egress) with the magnetic requirements (peak field strength and uniformity). Integrated Engineering Software's *MAGNETO* software was used to run magnetostatic calculations of axisymmetric cross sections of the coil assemblies. A trade-off study was performed to evaluate the effect of radial- and axial-separation of the two coils, as well as the number of turns required to meet the requirements. The coil design selected consists of two two-inch inner diameter coils, each with sixty four turns of 12 gauge square magnet wire. The G10 coil housings were designed to space the coils two inches apart, with the sample residing within the bisecting plane.

The coils are not truly a Helmholtz pair, as the coils are separated by a distance roughly equal to their inner diameter instead of their inner radius. The selected design met the space constraints and fulfilled the peak magnetic flux density requirements. Unfortunately, the uniformity constraint had to be relaxed to 2.3% over the 7mm sample radius.

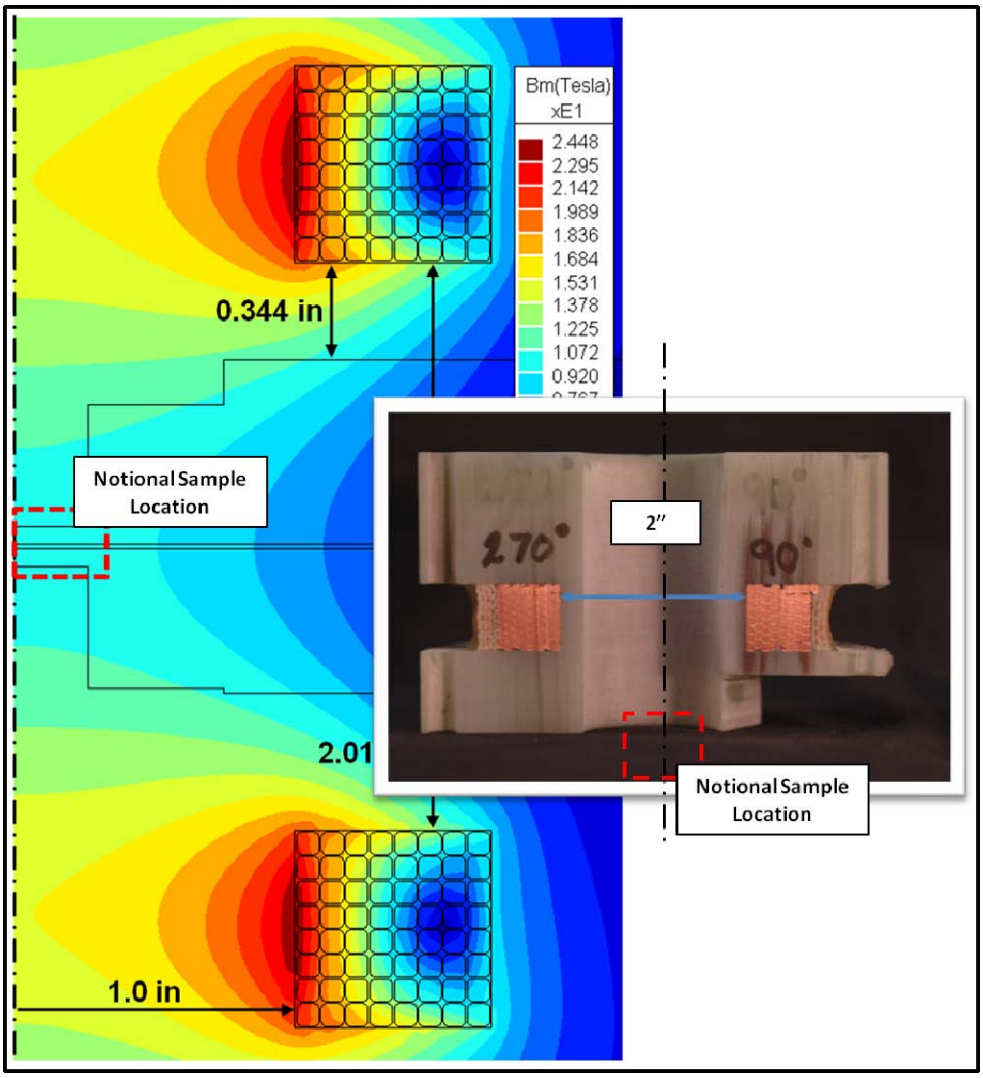

Figure 19: Magnetostatic flux distribution for I = 12.08kA (inset: single coil [top] cross-section)

Figure 19 shows the results from the magnetostatic simulation. Solid black lines indicate the location of the stainless steel VELOCE plates, which are assumed axisymmetric for the simulation. The implicit magnetostatic assumption effectively renders any object with finite conductivity to be transparent to magnetic flux, which is why the plate do not appear to perturb the field pattern. A closer inspect of the sample region (nominally within the dotted red block) shows that from r = 0mm (left side of figure) to r = 7mm, the field drops from 10.0T to 9.77T, roughly 2.3%. A uniform current density source is driven through each winding, whose accumulative behavior is equivalent to a drive current of 12.08kA energizing both coils in series.

The DC impedance of this coil point design is used earlier as the coil impedance in Figure 18. The calculated inductance (L_{calc} = 603μH) of the coil pair agrees very well with measurements made of the coil pair without the plates present (L_{meas} = 606μH). The calculated DC resistance values are close to those measured at test frequencies seen below in Table 2 (when coaxial cable transmission lines are subtracted from the measurement), suggesting that there are not significant

AC proximity effects between the coil windings that would otherwise increase resistance with drive frequency.

With a representative circuit model, current profiles can be simulated for the system. Bulk body forces can be estimated on each coil based off peak current numbers. Sandia's SLINGSHOT code [30] calculated the maximum radial outward-directed force on a coil's windings to be 1.026MN for a current pulse with peak amplitude of 12.3kA. A composite overwrap is required to contain the windings during the current pulse. Using equations for calculating stress from a uniform internal radial pressure on a thick walled vessel [31], it was determined that a 10mm thick outer shell of 70% fill Zylon would experience a peak hoop stress of about 1GPa. With an estimated ultimate strength at room temperature of 3.5GPa [32], the outer wrap is expected to contain the coil windings for the lifetime of a coil pair.

Figure 20 shows the coil pair mounted onto a surrogate VELOCE test plate assembly. Each coil is fitted with a header that transitions from the coaxial YK-198 pulsed power cable to the 12 gauge square magnet wire. Each coil is fed by its own YK-198 cable. A separate cable header is required to put these cables in series to be driven by the MPG capacitor bank cabinet.

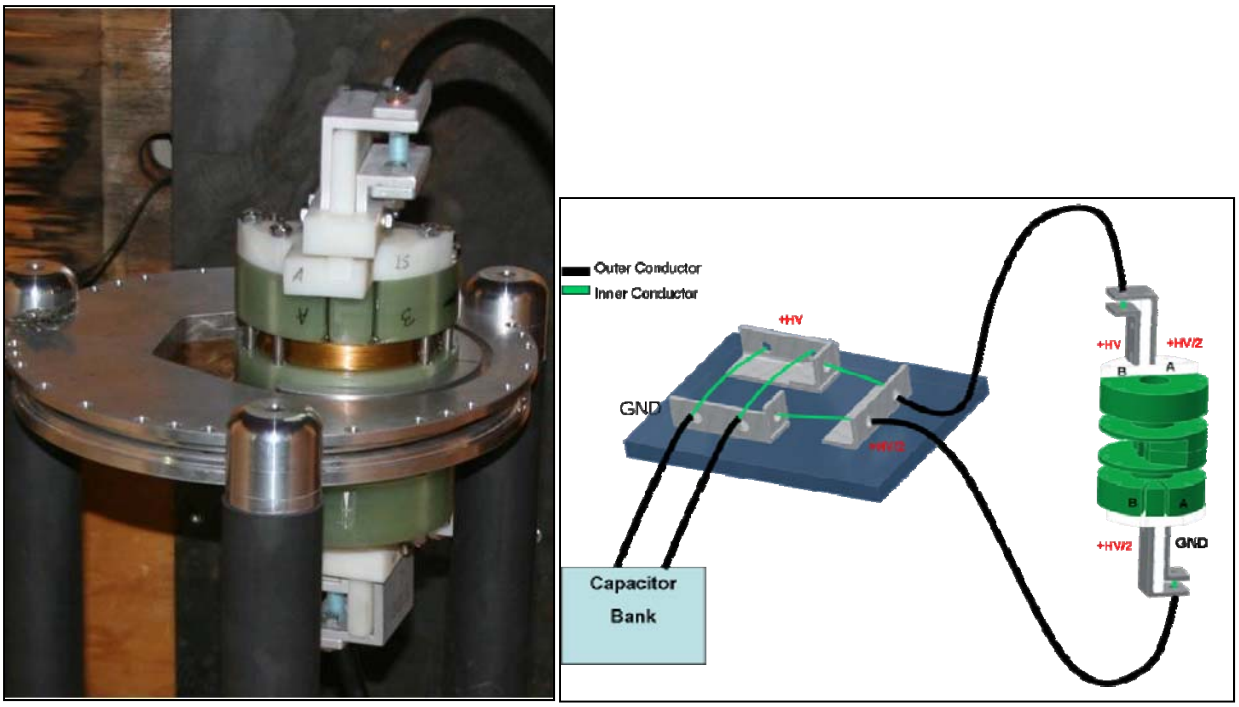

Figure 20: Coil pair mounted onto VELOCE plates (left). Cable header that serializes cables (right)

The outer jackets of the coil cables are pinned to half the instantaneous voltage across the coil assembly during the current pulse because of voltage division across identical coil impedances. Care must be taken to ensure that these cables are isolated from any conductors during their ingress into the VELOCE test chamber.

Impedance measurements can be made at the +HV and GND terminals seen on the right half of Figure 20, with the capacitor bank YK-198 cables removed. Impedance bridge measurements

measure the series R-L impedance at a test frequency presented by the coils and their mutual coupling and both lengths of cable. Each coil header cable is 10ft long. YK-198 cable has characteristic resistance of approximately 2mΩ/ft and inductance of about 31.9nH/ft, which adds ~40mΩ and ~0.6μH to the system load impedance. Using an HP4912A Impedance Analyzer and measuring the series RL impedance, the following data was collected at five test frequencies.

	Measurement 1		Measurement 2		Average	
f (Hz)	L (μH)	R(mΩ)	L (μH)	R(mΩ)	L (μH)	R(mΩ)
50	607	163	607	163	607	163
100	606	163	606	163	606	163
150	606	164	606	164	606	164
250	605	168	605	168	605	168
500	605.1	184	605.1	185	605.1	184.5

Table 2: Series R-L measurements made at cable header assembly

The undamped natural frequency f_o of the MPG system can be estimated using the following equation:

$$f_o = \frac{1}{2\pi\sqrt{LC}} \tag{3}$$

Where L is the dominant inductance in the circuit (load coils, nominal 605μH) and C is the dominant capacitance (parallel capacitor bank, or 9mF). A fundamental frequency of 68Hz is estimated, suggesting that the measured impedance values for 50Hz and 100Hz are sufficiently accurate for modeling the impedance of the load coil in lumped circuit equivalent models.

Integration into MPG Cabinet

The interface between the capacitor bank and the coils occurs at the cable header assembly, where two parallel YK-198 cables connect from the capacitor bank. The pulsed power equipment detailed in Figure 22 was placed in a cabinet along with the remote controller chassis that enables a user to remotely operate the MPG system from a control room.

Figure 21 was created to align the circuit components as they are laid out in the cabinet. The power supply and its limiting resistors and projection diodes are on top, above the thyristor switch stack. In front of the switch assembly are the charge and dump relays and charge fuse. The four capacitors are at the base of the cabinet. The dump resistors are mounted to the side of the cabinet and are not visible in the image.

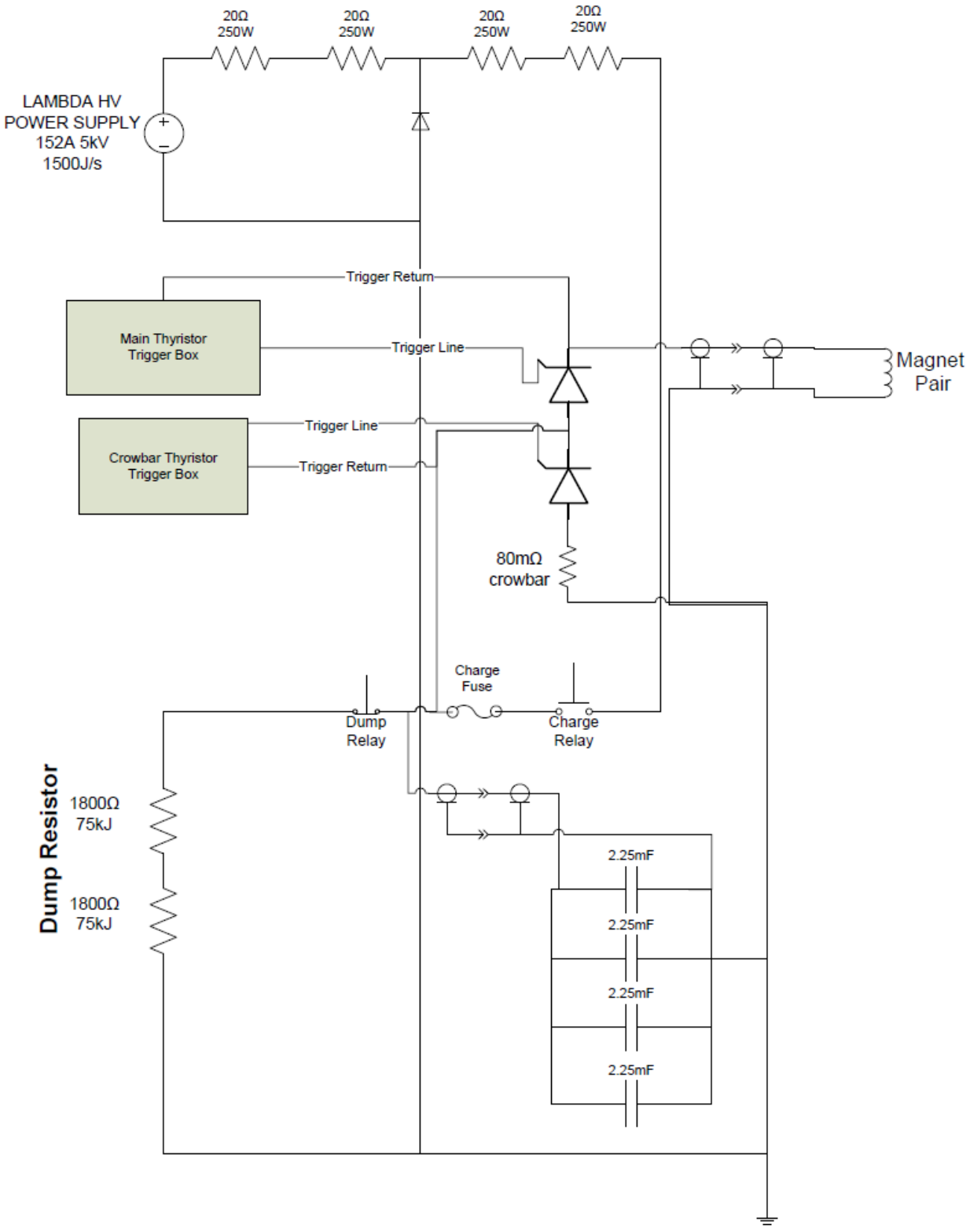

Figure 21: MPG pulsed power circuit schematic as arranged in cabinet

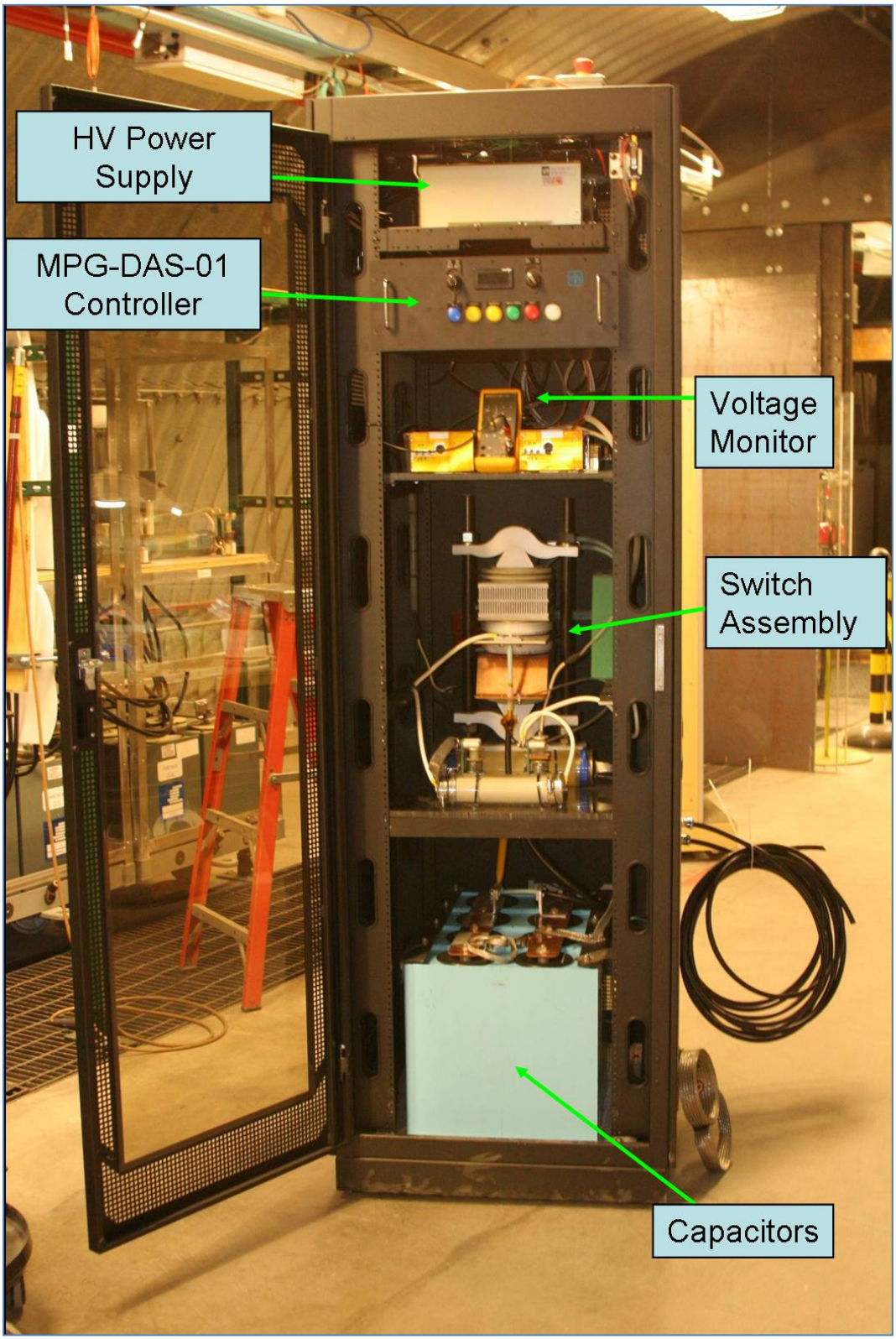

Figure 22: MPG cabinet with main components indicated

4.2.2. The MPG Control System

Figure 23: MPG-DAS-01 controller chassis front (top) and back (bottom) panels

Seen in Figure 23 above, the Magnetic Pulse Generator Data Acquisition System (MPG-DAS-01) Controller was developed to provide remote control of the MPG capacitor bank from a control screen room via fiber optic link. A control program was written in National Instruments LabVIEW® to control the charging and firing of the capacitor bank system from the VELOCE screen room.

B&B Electronics EIR205-MT media converters were used to convert the Ethernet-based communication between the experimenter and controller via a fiber optic data link. An Adam-5000/TCP distributed input/output controller was used as the primary I/O point for local communication with the HV power supply and opening/closing the charge/dump relays. A Highland Technology T-560 Embedded Digital Delay Generator provides two TTL pulses to precisely synchronize the triggering of the main and crowbar thyristors. A third channel of the delay generator is used to trigger the VELOCE system near the time of peak MPG current.

The two delay generator pulses are converted to optical pulses and transmitted via fiber to the thyristor trigger boards. These boards are electrically isolated from the control system because the circuit boards and their enclosures are required to float to the potential of the thyristor they are triggering. In Figure 21, the Crowbar Thyristor trigger box floats to the charge voltage of the capacitors before triggering.

A Xytronix "Control By Web" ethernet-controlled relay module was installed into the MPG-DAS-01 system to allow remote control of power state of the HV power supply. This change was made to prevent power supply damage in the event of a VELOCE prefire during MPG charging. The following figure provides a high-level block diagram of the hardware within the controller chassis.

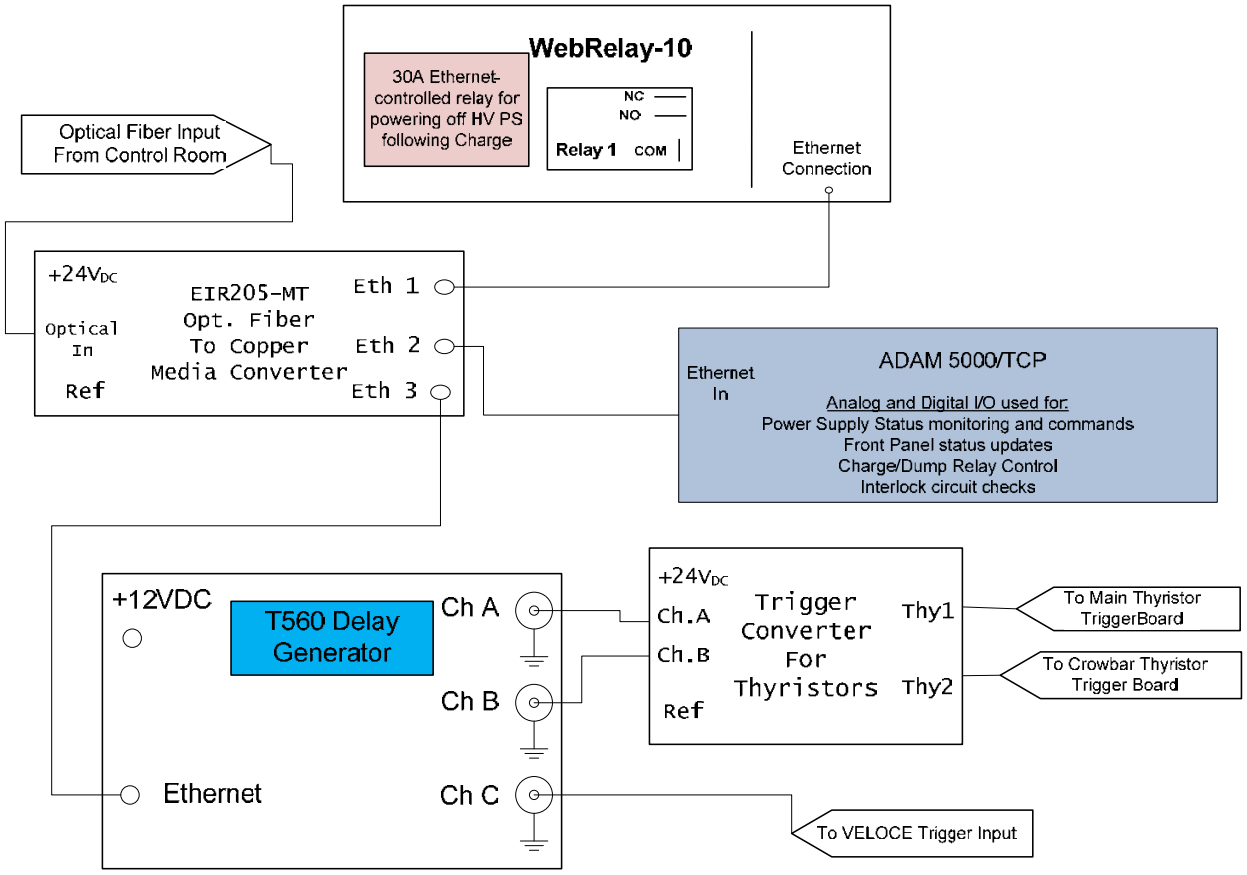

Figure 24: High-level block diagram of MPG-DAS-01 control system

To run the MPG system, the user first starts the LabVIEW® Virtual Instrument (VI) control program. The user sets the desired charge voltage, trigger times for the main and crowbar thyristor switches, and time delay to sending the reference pulse to the VELOCE experiment (with respect to firing the main thyristor). To minimize voltage reversal on the capacitors, typical values for main and crowbar thyristors switches are 0ms and 4.5ms, respectively. These settings are uploaded to the controller by pressing the Update Parameters button.

When the CHARGE command is pressed, the power supply begins to charge the capacitors at a constant rate of 1500J/s. The User can ABORT the charging sequence at any time. An ABORT command disables the power supply and resistively discharges the capacitors through the dump relay, dissipating the energy into a bank of resistors rated to handle 150kJ. The MPG system can be fired only when the power supply has reached the voltage setpoint and output its "End of Charge (EOC)" indicator. Via the relay module, the power supply can be turned off once EOC has been reached. A FIRE command isolates the power supply and fires the delay generator, starting the thyristor triggering sequence. Figure 25 graphically provides program flow of the MPG-DAS-01 control program.

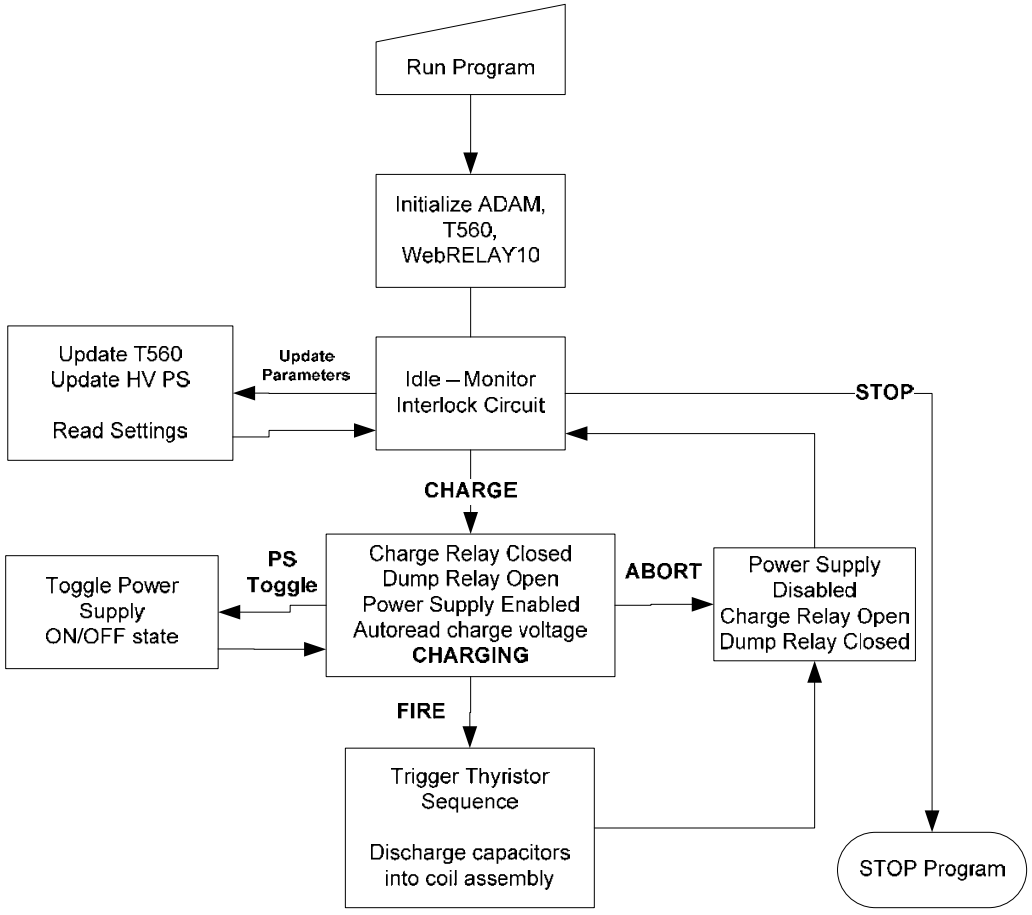

Figure 25: MPG-DAS-01 Control Program Flow

The MPG cabinet also contains current and voltage diagnostics that are returned to the control room via standard RG-58 coaxial cable. A current monitoring probe with sensitivity of 0.5mV/A is installed to provide the user with the current history of a given pulse. A DC high voltage probe is directly connected to the capacitor HV bus to provide a measurement of capacitor voltage. This signal is also available to the control room via a RG-58 coaxial signal cable.

4.2.3. Testing and Commissioning of the MPG System

The MPG bank system needed to be vetted as a pulsed power system before integrating into the VELOCE system. Likewise, the coils needed to demonstrate the ability to survive the mechanical loading of the design current at least until after peak current has been reached. The following section details the testing performed in 2009 to answer these questions.

Early MPG Commissioning and Coil Testing

In November 2008, an intensive testing campaign of the MPG system was performed prior to deployment on VELOCE. The capacitor bank had to demonstrate the ability to operate at the required voltage and current levels before system delivery. Prior to ever firing the capacitors into a load, each node of the circuit passed a hi-pot test to ensure there were no unexpected breakdown paths that could short out the capacitor bank. The charge and dump process was tested to validate that the power supply could charge the capacitors to required test voltage. The dump resistor assembly was validated to dissipate all 110kJ of stored energy in an ABORT operation.

The aforementioned tests demonstrated compatibility with the required voltages. To demonstrate that the circuit can operate at the required electrical current (12.5kA into 600μH load), a surrogate 30μH coil was used. The MPG system was charged to 1.650kV and fired into the surrogate, achieving nearly 14kA and verifying that the hardware was sufficiently robust to handle required experimental currents.

In December 2008, the baseline coil design with Kevlar fabric overwrap was delivered for testing. A coil pair was tested in 0.5kV capacitor voltage increments until the overwrap failed during the 3kV test, cracking at coil current of 7kA. This current corresponded to roughly one quarter of the peak force calculated to occur at the max design point of 12.5kA. At this point, the coils were redesigned and prototyped with the zylon overwrap referenced in section 0 above, providing an expected safety factor of 3 at the peak force of 1.03MN.

In February 2009, a pair of Zylon-overwrapped coils was subjected to a series of current pulses. The seven shot series, whose current waveforms are presented in Figure 26, demonstrated that the new coil overwrap was sufficiently strong to survive up to 81% of structural loads. Shots 01-06 were system verification tests at low energies (no more than 16% of design energy). The final shot in the series was at 4.55kV, and demonstrated that the coil pair could handle that load without catastrophic failure. During this shot, the superstructure compressive assembly failed, resulting in minor coil damage. The superstructure needed to be rebuilt before a 5kV shot could be attempted. Following this test, it was decided to move directly to a coil pair mounted onto a surrogate set of VELOCE plates and perform full energy tests.

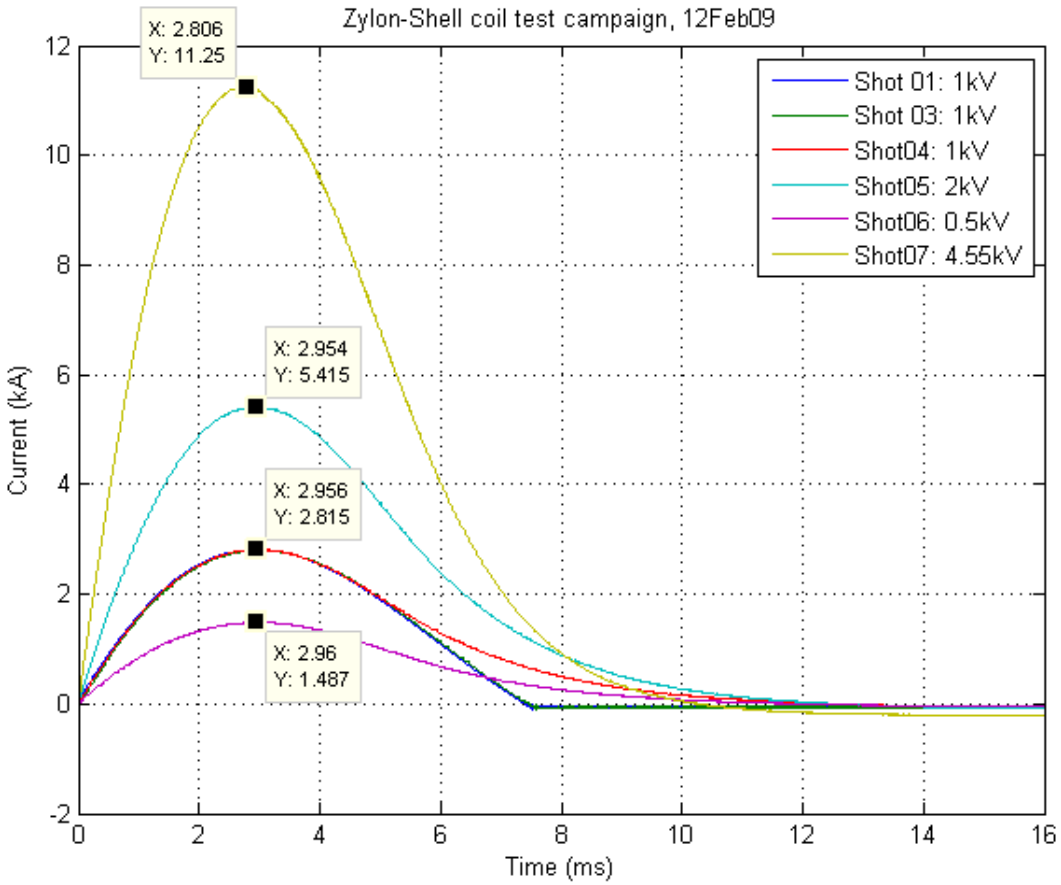

Figure 26: Current waveforms during zylon overwrap test campaign

MPG Coil Validation on Surrogate VELOCE hardware

The VELOCE team provided a structure that represented the plate assembly and spacing that would be seen in the VELOCE test chamber. The two plates were separated by sheets of kapton and test samples were installed to provide as accurate a magnetic environment as possible for the coil pair. The coils were tested with the coil header and cable header assembly. During May 2009, a series of test shots on a coil pair were performed, achieving three shots at approximately 5kV before the decision was made to move the MPG system to VELOCE.

Figure 27: Coil pair setup with test assembly (right) and cable header (left)

Figure 27 shows the coil pair and surrogate VELOCE plates in the test area. The MPG cabinet is out of frame to the left. The current waveforms for these full energy shots are presented in the following figure.

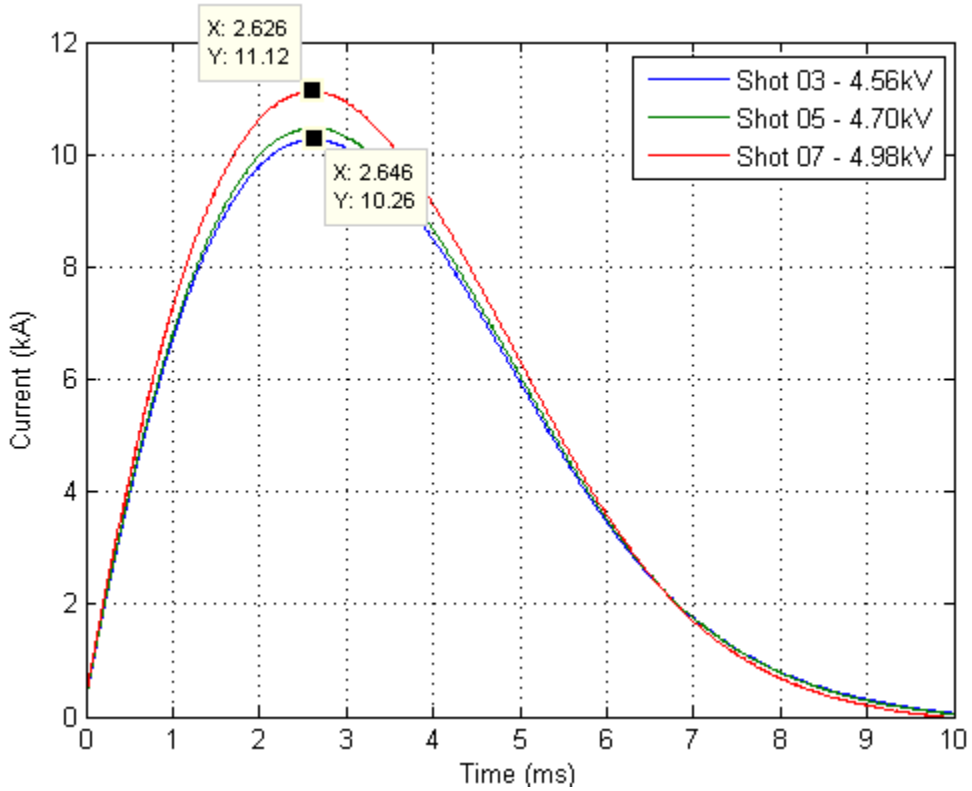

Figure 28: Current histories for coil pairs on surrogate VELOCE plate assembly

Inspection of Shot 07 data revealed an unfortunate result, that the maximum output of the MPG system was not achieving current levels sufficient to apply 10T to the sample. Following the design and implementation of the coil headers (that transition from magnet wire to coaxial pulsed-power cable) and cable header assembly, the addition of 20ft of YK-198 cable had increased the net resistance of the load to prevent reaching the required current to achieve 10T at the sample.

The additional cable length added 40mΩ to the transmission line impedance, further dampening the frequency response. Even accounting for this additional loss in the SLINGSHOT circuit model, the model still overshot reality, predicting a peak current 11.62kA for Shot 07 as seen in Figure 28. While the SLINGSHOT simulation code captures ohmic heating and subsequent increase in resistance for coil conductors, it does not account for resistivity increases from heating of transmission line conductor. Table 3 summarizes the change in transmission line resistance for different initial charge voltages.

Bank Voltage	Ipeak	Action	Heat Energy	ΔT	Resistivity Change	Final Resistance
kV	A	kA^2	J	K	%	mΩ
0.5	1175	4.3	170.4	0.8	100.52%	40.2
1	2349	17.0	681.6	3.1	102.08%	40.8
1.5	3521	38.3	1533.6	6.9	104.69%	41.9
2	4689	68.2	2726.4	12.3	108.33%	43.3
2.5	5853	106.5	4260.0	19.1	113.02%	45.2
3	7012	153.4	6134.4	27.6	118.75%	47.5
3.5	8007	208.7	8349.6	37.5	125.51%	50.2
4	9072	272.6	10905.6	49.0	133.32%	53.3
4.5	10110	345.1	13802.4	62.0	142.18%	56.9
5	11120	426.0	17040.0	76.6	152.07%	60.8

Table 3: Change in resistance of YK-198 cable for different current pulses

When the higher transmission line resistance is used in SLINGSHOT as a function of charge voltage, the circuit model agrees very well with experimental results during the current pulse rise time. The two current profiles begin to diverge after peak current, as the time dependent system resistance increases above the hardwired model resistance. The following table shows the modeling results before and after this parameter change. These results imply that MPG circuit behavior can be approximated very well by including a higher resistance for the transmission line, based on some *a priori* knowledge of the action for a given current pulse.

Charge Voltage	Experiment Current	Slingshot Current
(kV)	(kA)	(kA)
1.08	2.812	2.83
2.10	4.912	4.923
4.56	10.27	10.24
4.70	10.48	10.47
4.98	11.12	11.12

Table 4: Comparison of actual and experimental peak currents following model update

Predicting magnetic field strength at the sample

A three-dimensional model of the plate and the coil windings was created in Ansoft® Maxwell 3D magnetic solver. The following figure shows the geometry as it appears in the model. Maxwell 3D does not calculate structural response, so there was no need to model the G10 composite support structure. A symmetric boundary condition was applied to the XY plane to simulate the presence of the other plate and coil. The aluminum model used has a resistivity of 3.99μΩ-cm, to match the published resistivity of Aluminum 6061-T6 alloy. The copper model uses an electrical resistivity of 1.7μΩ-cm, though the magnet wire used was approximately 1.82μΩ-cm. This only effects the DC resistance calculation of the winding, and would only damp the resistance further. No eddy effects are calculated for stranded conductors, which the coil is modeled as within Maxwell 3D.

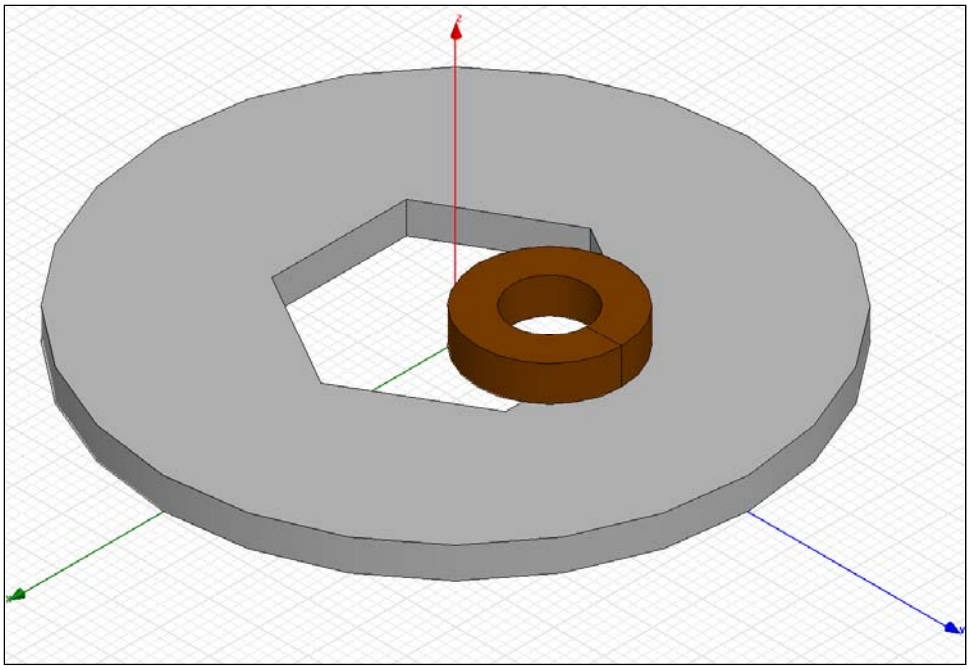

Figure 29: Maxwell Simulation Geometry: Copper winding (brown) and VELOCE hex plate (gray) are shown

A transient solution was run with the coil coupled to an external capacitor circuit to best approximate the VELOCE-MPG capacitor bank. The discharge of this capacitor into the FEA coil winding reasonably approximates the current pulse seen during an MPG 5kV discharge. Maxwell does not perform an element-by-element update of material resistivity as a function of deposited ohmic energy, which would damp the current behavior by increasing the resistivity of the coil windings.

A series resistor and an inductor were added to include the effects of the YK198 transmission cables. The external circuit coupled to the magnet is shown in the following figure.

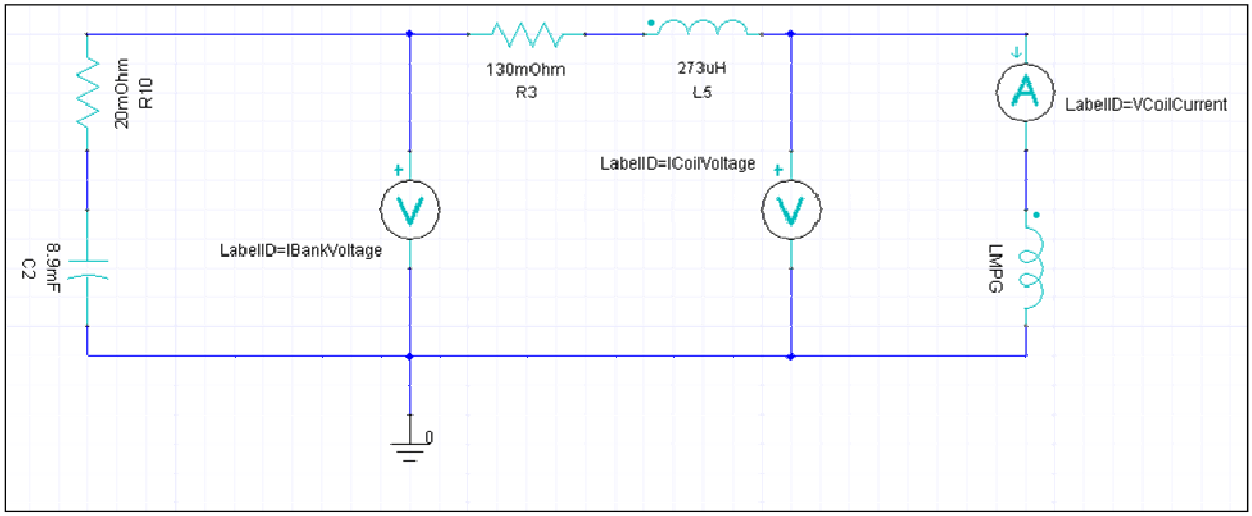

Figure 30: Simple lumped-circuit equivalent for MPG capacitor bank used in Maxwell Simulation

The crowbar switch circuit branch and its equivalent resistance and inductance were left out of the bank circuitry for simplicity. The 8.9mF capacitor has an initial condition of 5kV. Coil current is forced to have 0A initial current. The circuit rings and establishes a magnetic field comparable in intensity and spectral content to that of the experimental data.

While the circuit response does not have the complexity or accuracy of the SLINGSHOT model mentioned earlier, the magnetic field calculated on the sample at time of peak current will scale linearly with peak current. This conclusion assumes that the magnetic field has diffused through the sample and plate well within the rise time of the current pulse, which inspection of the transient simulation confirms. A tabulation of peak current versus initial capacitor voltage can be created from experimental data and verified with Slingshot simulation results. Then, the magnetic field calculated at the sample can be scaled to the appropriate level based on ratios of current. Figure 31 provides predicted peak current and magnetic field values as a function of capacitor voltage. The Maxwell 3D results suggest that the 11.12kA pulse at 5kV is nearly achieving 10T.

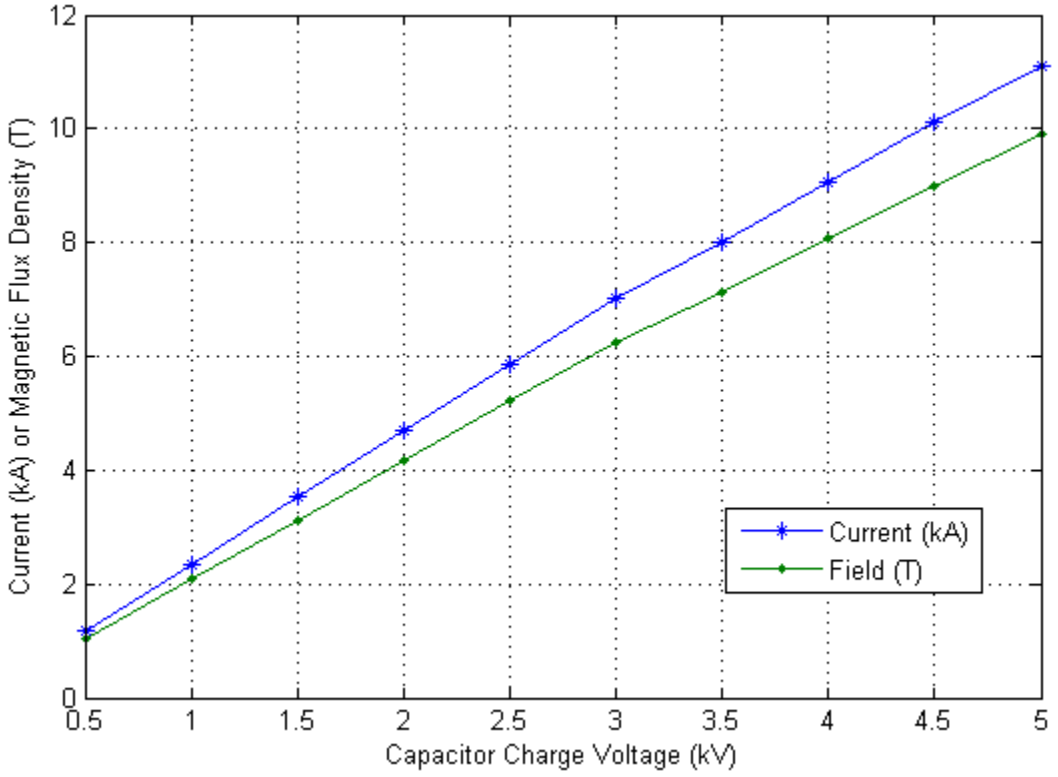

Figure 31: SLINGSHOT-predicted peak current and Maxwell 3D-calculated magnetic flux density at sample

4.2.4. Future Work With the MPG System

There is some potential for future work with the Magnetic Pulse Generator system. The capacitors can be upgraded to a higher capacitance or higher rated voltages to increase the amplitude of the current pulse that a given coil design can achieve. A parameterized transient

simulation could be used to find the optimal coil spacing and inductance to achieve higher, more uniform fields on the sample.

A closer look at the coupling between VELOCE and MPG is warranted, as pulses induced on the MPG system by VELOCE operation are damaging MPG equipment. A detailed look at inductive chokes or circuit snubbers to protect the thyristor switches from VELOCE feedback would improve switch lifetime. Redesigned thyristor trigger boards that include protection from induced noise is desirable. Eliminating batteries from the thyristor trigger board design would improve test turn-around and system troubleshooting. These improvements would be required before MPG or a similar system could be deployed on a larger pulsed power machine.

4.2.5. Timing with Veloce

In order to achieve the desired results, care was taken to ensure the correct timing of the MHD drive relative to the MPG pulse. Figure 32 shows the MPG current pulse and the Veloce system trigger. A delay of 92 ms was used following the MPG trigger prior to triggering Veloce. This resulted in the MHD drive occurring just prior to the fall off from peak of the MPG current. This allowed time for the external magnetic field to permeate the sample region (including the drive panels).

Figure 32 also indicates the feedback discussed in the previous section. The MHD drive current feeds back into the MPG via the magnet power supply lines and results in the rapid shift to a negative going current as detected by the MPG current sensor.

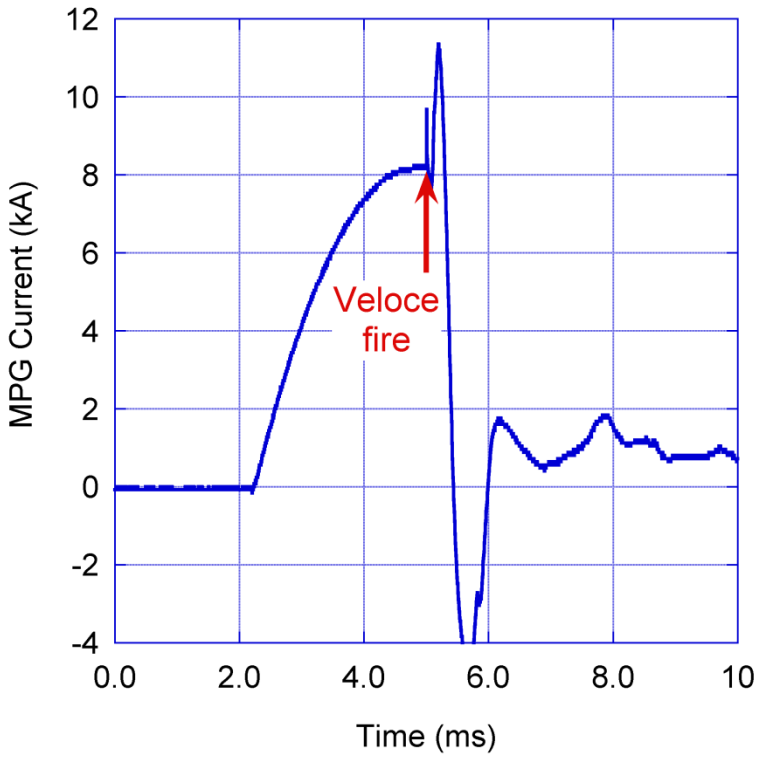

Figure 32: MPG current from shot MS-10. Arrow indicates the time of Veloce fire (MHD drive).

4.3. Transverse VISAR

In order to measure the shear waves present in these experiments, a diagnostic sensitive to transverse effects was required. A transverse capable VISAR system was selected based on the existing technical expertise with longitudinal VISAR measurement at Sandia. The transverse capable VISAR system is based on a design by Chhabildas and Swegle [33]. The implementation has been modified to allow the use of fiber optic probes in place of open beams. The system relies on three probes as illustrated in Figure 33. Normally incident light (probe 3) is reflected from the diffuse sample surface and in collected by two additional probes (probes 1 and 2) set at angles θ_1 and θ_2 respectively as shown. The light is then directed through a standard push-pull VISAR cavity to determine the apparent velocity at each angle.

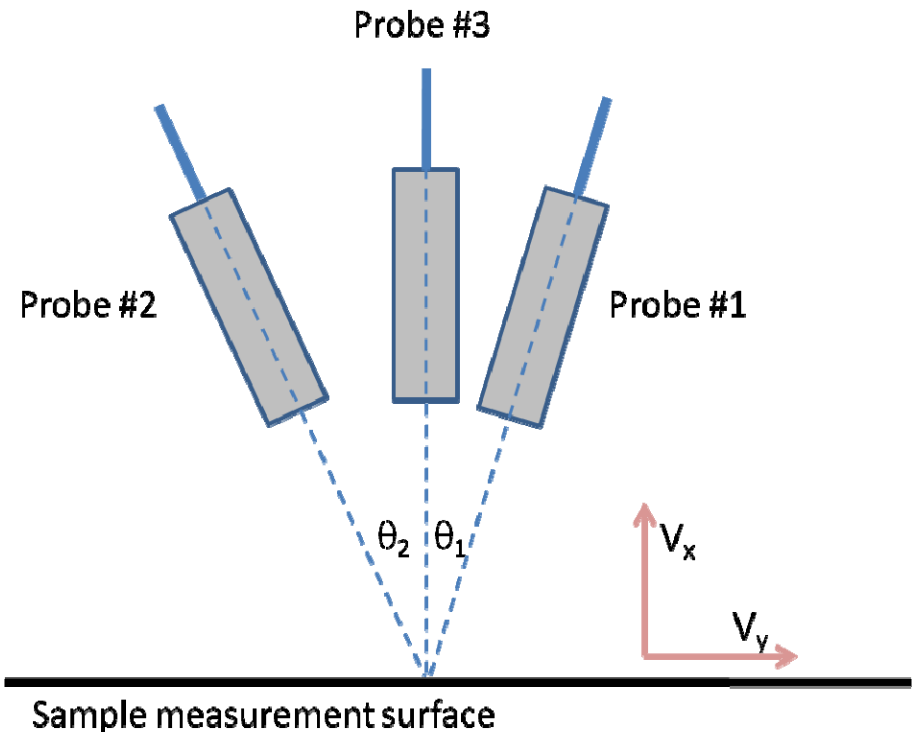

Figure 33: Illustration of the transverse capable VISAR diagnostic.

The apparent velocity (v*), in terms of the actual longitudinal (v_x) and transverse (v_y) velocities, is determined by the angle of the collection probe:

$$v_i^* = v_x\left(\frac{\cos\theta_i+1}{2}\right) + v_y\left(\frac{\sin\theta_i}{2}\right) \quad (4)$$

This expression holds for each collection probe noted by the subscripts 1 and 2. Thus, by combining the results from two probes the system is determinant and longitudinal and transverse velocity is found from:

$$G_1 = \frac{1}{2}(\cos\theta_1 + 1)$$

$$G_2 = \frac{1}{2}(\sin\theta_1)$$

$$G_3 = \frac{1}{2}(\cos\theta_2 + 1)$$

$$G_4 = -\frac{1}{2}(\sin\theta_2) \quad (5)$$

$$F_1 = G_1 - \left(\frac{G_1 G_2}{G_4}\right)$$

$$F_2 = \left(\frac{G_2}{G_1 G_4 - G_2 G_3}\right)$$

$$v_x = \left(\frac{v_1^* - F_2 v_2}{F_1}\right)$$

$$v_y = \left(\frac{v_2^* - F_3 v_x}{G_4}\right)$$

where G1, G2, G3, and G4 are geometric constants determined by the angles of the collection probes relative to normal. The factors F_1 and F_2 combine the geometric constants and are shown to enhance the readability of the equations. In this notation, the angles θ_1 and θ_2 are positive numbers; the effect of the negative θ_2 is explicitly shown. The direction of θ_1 is the positive v_y direction.

Collimating fiber optic probes from Oz Optics were used for these experiments. Collimating probes are designed such that light emitted from the probe travels parallel to the axis of the probe. This is in contrast to a more typical focusing probe which, as the name implies, focuses emitted light to a point. Collimating probes were used to ensure that light collected was reflected at a fixed angle from the sample. Only light rays parallel to the axis of the probe will be collected and transmitted to the VISAR system. In practice, there is a slight divergence angle determined by the numerical aperture of the fiber and the lenses in the probe. This effect increases the experimental uncertainty slightly but a sensitivity study showed that the effect is small.

A series of tests were conducted to verify the proper operation of the transverse VISAR system. Plate impact tests using y-cut quartz targets were used. Impacting y-cut crystalline quartz results in both longitudinal and transverse waves in the target due to crystal anisotropy [33]. Results are shown in Figure 34 along with simulation results from Laslo, a 1-dimensional, Lagrangian shock physics code [34]. Agreement between the experiment and simulation is acceptable. Differences are most likely due to deficiencies in the model used for the quartz in the simulation. A standard longitudinal VISAR probe was also fielded and agreement between this result and the longitudinal velocity determined from the transverse capable VISAR is excellent. This agreement supports the argument that there was a deficiency in the calculation.

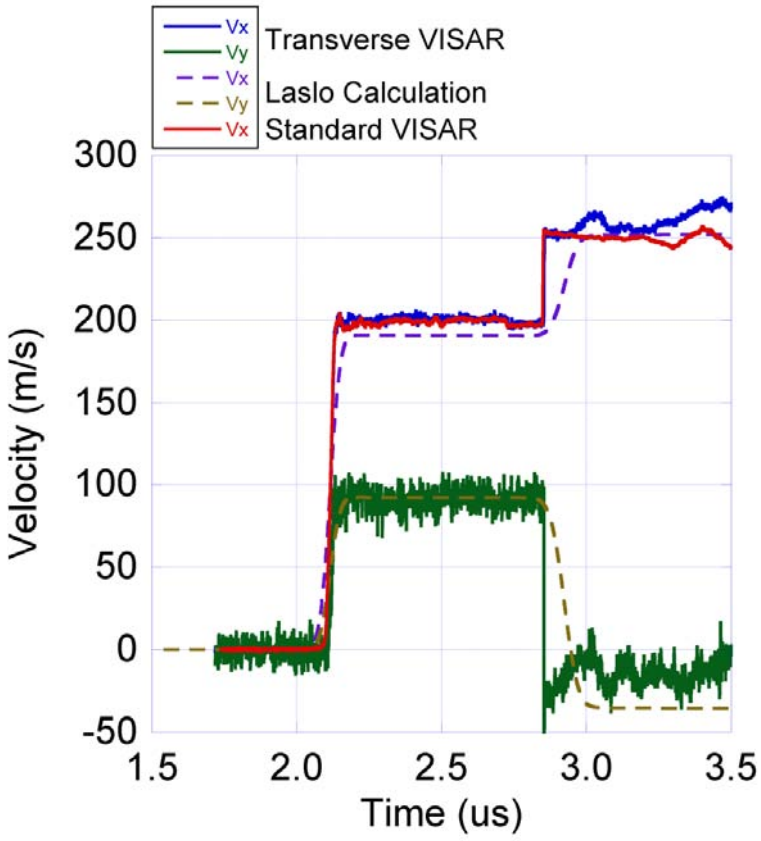

Figure 34: Resolved longitudinal (v_x) and transverse (v_y) velocities from a test of the transverse VISAR system. Also shown are simulation results from Laslo and recorded longitudinal velocity from a standard VISAR. Note that the velocity subscripts refer to the longitudinal and transverse directions, not the quartz crystallographic axes. In this test, the crystallographic x-axis was aligned to the measurement y-axis (transverse direction).

A null test was also conducted. A similar plate impact of y-cut quartz was conducted. The transverse capable VISAR probes were rotated 90 degrees from the previous case in order to measure transverse velocity along the crystallographic z-axis. There is zero expected motion in this direction. The results shown in Figure 35 indicate a small transverse velocity. Simulation results indicate the recorded motion is expected for a six degree misalignment of the probes to the z-axis. This amount of error is possible as no precise mounting fixture was used and orientation markings on the sample were subtle. While the results did not indicate zero motion, they do show that the system is capable of detecting transverse motion on the order of 10 m/s with an uncertainty of about 3 m/s. This low threshold is important as the system will be suitable for use when using MAPS to measure samples with low strength.

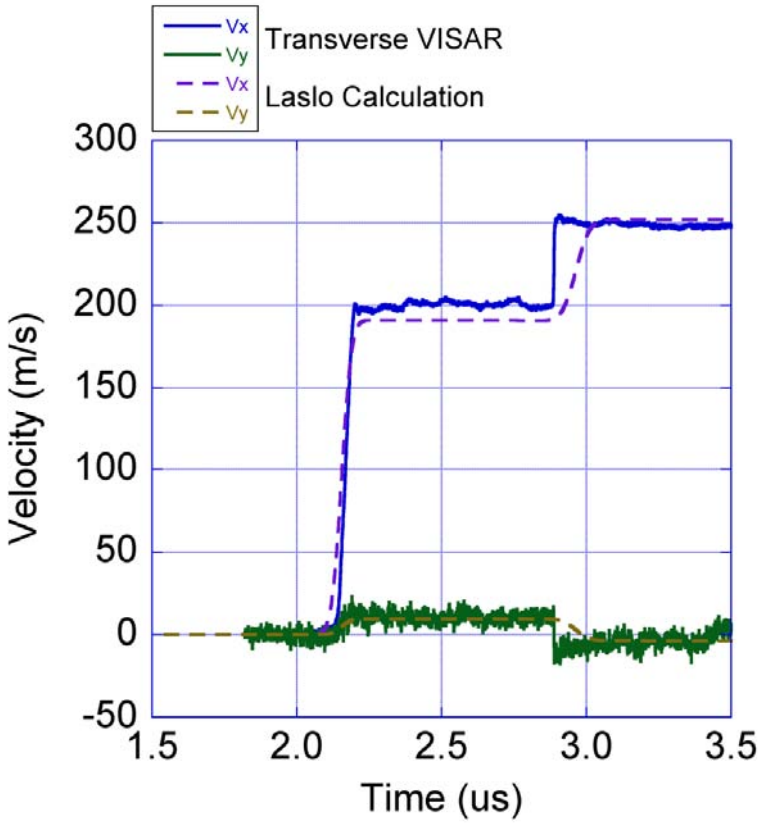

Figure 35: Resolved longitudinal (v_x) and transverse (v_y) velocities from a test of the transverse VISAR system. Also shown are simulation results from Laslo. Note that the velocity subscripts refer to the longitudinal and transverse directions, not the quartz crystallographic axes. In this test, the crystallographic z-axis was about 6 degrees off the measurement y-axis (transverse direction).

4.4. Material Preparation

Sample preparation is important to any experiment. MAPS experiments present some unique challenges due to the combined effects of pressure and shear. In a compression only experiment, material interfaces are required to be flat and parallel, generally to tolerances of the order of 100-200 nm. This allows for excellent transmission of compression waves with minimal effects arising from gaps or other interface defects. When shear is involved, smooth, flat interfaces have been shown to be detrimental as the glue bond between materials is insufficiently strong to support shear in excess of about 0.35 GPa [33]. Increased surface roughness will allow for better shear transmission as demonstrated by a series of ALEGRA calculations detailed below. Due to the importance of shear transmission, a great deal of attention was paid to the development of a suitable compromise for surface roughness.

4.4.1. Simulation results regarding surface roughness

A series of calculations were performed to investigate the effect of surface roughness on shear transmission at a boundary. The problem was simulated with a molybdenum driver bonded to an aluminum sample with a triangular shaped interface with peak-valley magnitude of 1, 2, or 3 μm

and a wavelength of 2 μm, as shown in Figure 36 for the 1μm amplitude case. The simulation also included a glue bond layer 1 μm thick. These thicknesses were chosen to span the typical range for parts used in Veloce experiments. Cell size is 0.05 microns. The driver and sample thicknesses were 1 mm each to prevent and perturbing boundary effects. To limit computational requirements, the simulations were run using solid-dynamics only, not MHD. The left-hand boundary was driven with a traction boundary condition using stress components that were taken from an MHD simulation at 1 mm before the interface, to replicate the MHD drive. Tracers placed on either side of the boundary measure shear wave magnitude. Results indicate no reduction of shear wave transmission across the boundary as the surface roughness is decreased through this range. Results show that the glue is compressed by the longitudinal wave, resulting in nearly direct contact of the driver and sample surfaces, removing the effect of the glue bond before the arrival of the shear wave. Based on these results, the minimum surface roughness desired was 1 μm or 1000 nm for the experimental interfaces although additional simulations with smaller interface roughness might reduce this value.

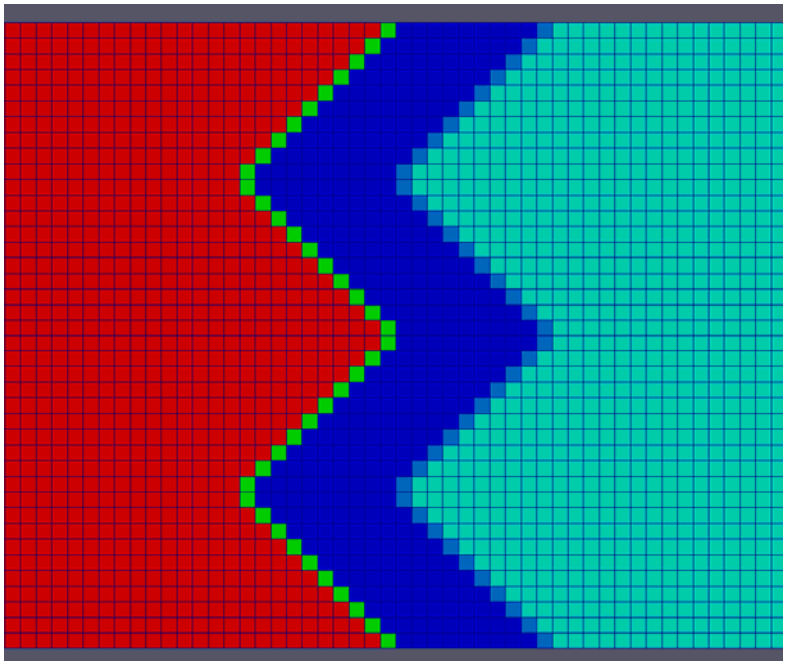

Figure 36: Partial view of the simulation domain for investigation of shear stress transmission across a material boundary. The case shown has a triangular surface interface with 1μm amplitude and 2μm wavelength. The glue bond width was 1μm.

4.4.2. Surface preparation

The material interfaces of concern are the driver-sample and sample-anvil interfaces. Both are assumed to respond similarly to the simulation results despite the fact that the anvils are made of zirconia as both molybdenum and zirconia are much harder and stronger than the aluminum sample.

The molybdenum drivers, as received, have an average surface roughness that varies from about 400 to 500 nm but can be as high as 1200 nm. In order to increase the roughness, the surface was bead blasted with a 240 grit (70 μm) SiC abrasive. This treatment increased the average roughness to 600 nm and resulted in much greater uniformity. Although a 1000 nm roughness was desired, additional blasting with the SiC abrasive resulted in no increase in the roughness. Shear transmission through a boundary with this surface roughness was tested experimentally. Results indicated complete transmission. Hence, this preparation was selected as the standard treatment for the molybdenum.

The zirconia anvils had an average surface roughness of only 1.4 nm as received. A similar treatment with 240 grit SiC abrasive was used resulting in a similar surface roughness of 600 nm. Again, this was less than the desired roughness of 1000 nm but deemed acceptable following experimental testing of shear transmission.

No preparation was performed on the sample surfaces. The sample thickness, on the order of 100 nm, prohibits the use of abrasives. In the case of pure aluminum, the material is also very soft and will assume the surface profile of the mating surface upon pressing of the materials during the gluing procedure. Further, as indicated by the simulation results, the compression wave will drive the material interface to conform to the rougher surface prior to the arrival of the shear wave. Thus, even for harder sample materials, no pre-treatment is expected to be required.

4.4.3. Reflective surface for VISAR

The transverse VISAR system requires a diffuse surface in order to reflect light to the off-axis collection probes as detailed previously. The 1.4 nm average roughness on the as received anvils was not sufficient. For simplicity, the identical treatment used for the sample-anvil interface side of the anvil was applied to the free surface increasing the average roughness to 600 nm. This surface was then coated with 300 nm of vapor deposited aluminum resulting in a diffuse reflecting surface found to be suitable for the VISAR system.

5. EXPERIMENTAL RESULTS

Three successful MAPS experiments have been conducted to date. Two of these served as proof-of-principle demonstrations measuring the strength of pure aluminum. The third was an anvil characterization test which resulted in experimental wave speed data for the zirconia anvils used. The data and subsequent analysis presented here should be considered preliminary as there have been a limited number of tests. As further results allow for refinement of critical parameters, such as anvil wave speeds, and advances in instrumentation permit reduction in the experimental uncertainty, subsequent results will be more accurate.

Two tests, shots MS-10 and MS-11, were conducted to demonstrate the technique using nearly identical conditions except B_o fields were chosen as 7 T and 5 T, inducing maximum shear stresses of 0.57 GPa and 0.40 GPa in the driver. This was done to demonstrate that the magnitude of the transmitted shear wave through the sample was independent of induced shear stress, providing it exceeds the sample strength (~0.4 GPa at these longitudinal stress levels).

5.1. Proof-of-Principle Shot MS-10

The experimental configuration for shot MS-10 is shown in Figure 37. The external magnetic field for this shot was 7.7 T resulting from a peak current of 8.23 kA from the MPG supply charged to 3.65 kV.

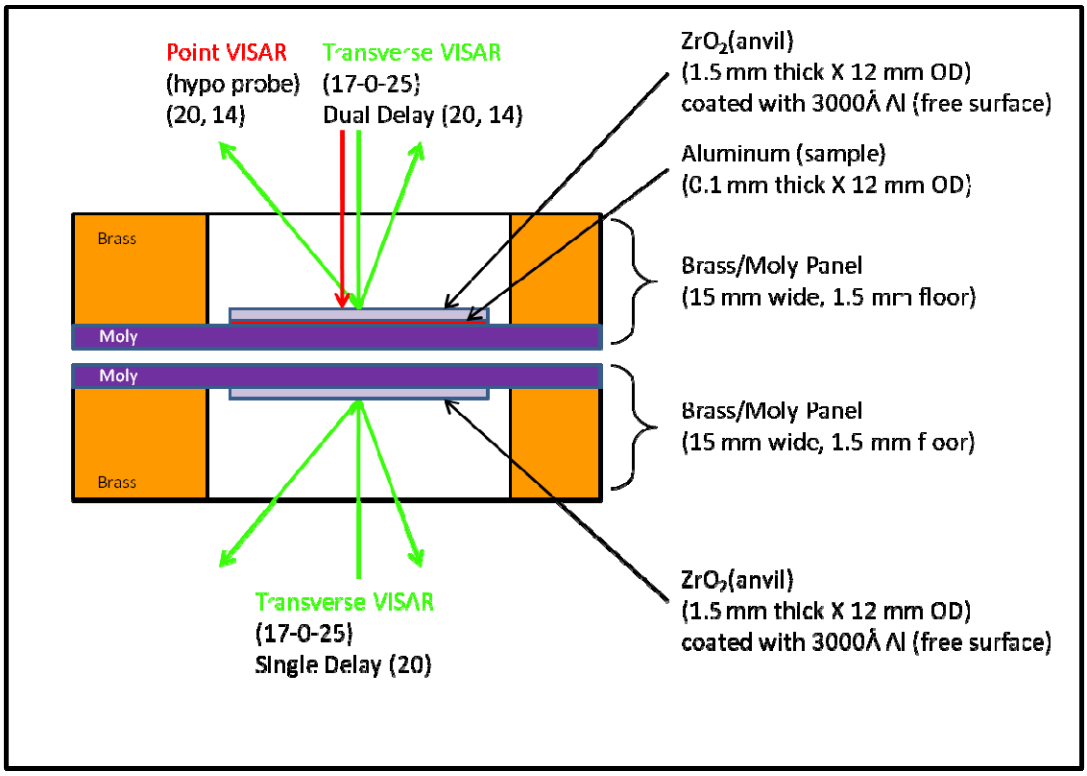

Figure 37: Experimental configuration for shot MS-10.

Figure 38 shows the apparent velocities recorded by the VISAR system. Following the approach detailed in section 4.3 above, longitudinal and transverse velocity profiles were determined from the apparent velocities and are shown in Figure 39. Comparing the results from the top (Al sample) and bottom (no sample) panels demonstrates that the sample truncates the input shear. The peak longitudinal velocity is essentially invariant while the peak transverse velocity is greatly reduced by the sample strength.

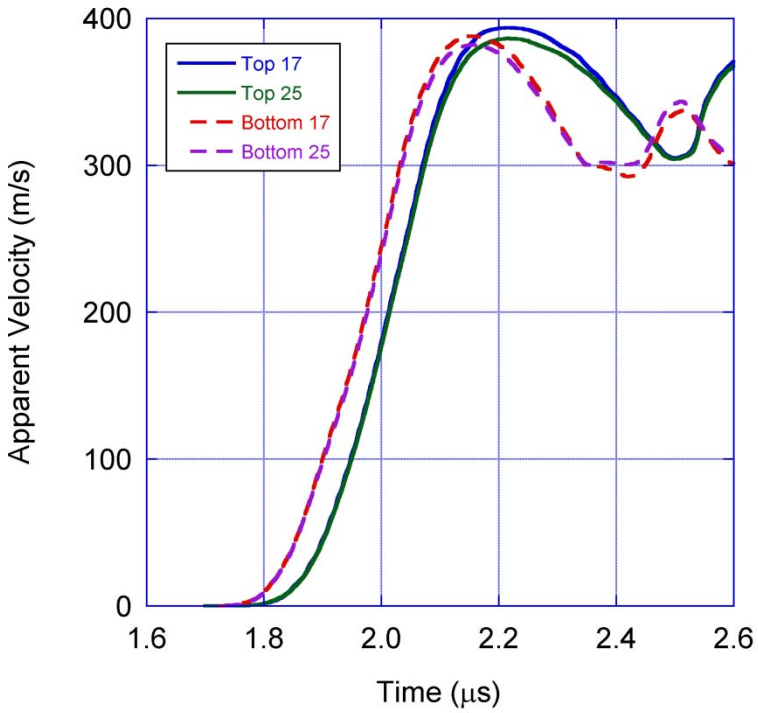

Figure 38: Apparent velocity recorded by the VISAR system for shot MS-10. Numbers in legend refer to the data collection probe angle. The top panel has an aluminum sample. The bottom panel has only the driver and anvil.

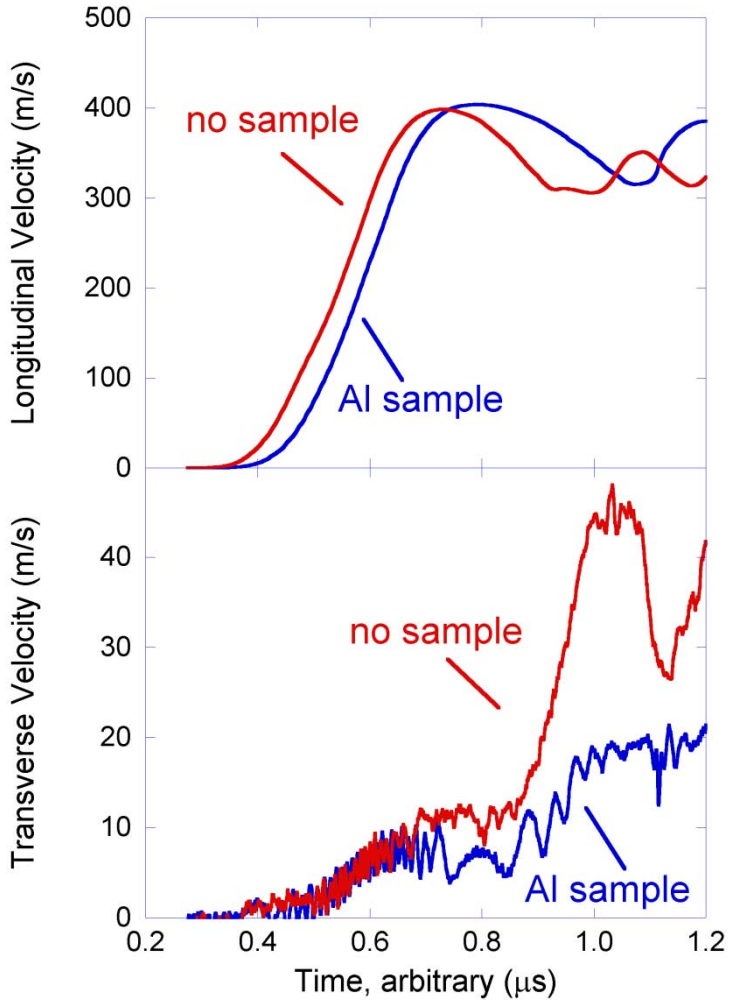

Figure 39: Resolved longitudinal and transverse velocities for shot MS-10.

The velocity profiles shown were measured at the free surface (fs) on the back of the anvil. *In-situ* particle velocity, u_p, is determined as $u_p = \frac{1}{2} u_{fs}$, from u_{fs}, for both the longitudinal and transverse velocities. Longitudinal and shear stresses, σ and τ respectively, are then determined from:

$$\sigma = \rho_o C_L u_p^{\text{longitudinal}} = \tfrac{1}{2} \rho_o C_L u_{fs}^{\text{longitudinal}} \quad (6)$$

$$\tau = \rho_o C_S u_p^{\text{transverse}} = \tfrac{1}{2} \rho_o C_S u_{fs}^{\text{transverse}} \quad (7)$$

where C_L and C_S are the Lagrangian longitudinal and shear wave velocities, respectively, in the anvil and ρ_o is the initial anvil density, measured to be 6.07 g/cm^3. Wave speeds in the anvil were determined experimentally from a companion shot using standard techniques discussed later and elsewhere [35]. Results indicate C_L = 7330 m/s and C_S = 4105 m/s. At these stress levels, the zirconia remains elastic [36].

The longitudinal and transverse free surface velocities were found to be 398.0 ± 3 m/s and 18.7 ± 3 m/s with the aluminum sample present and 399.3 ± 3 m/s and 46.0 ± 3 m/s without the sample. Inserting these values into equations 6 and 7 results in longitudinal and shear stresses of 8.85 GPa and 0.23 GPa for the aluminum sample case and 8.85 GPa and 0.57 GPa without the sample. Thus, significantly more shear stress was generated in the driver than was transmissible through the aluminum sample indicating that the observed shear stress was limited by the aluminum strength.

The strength of the aluminum sample was found to be 0.403 ± 0.064 GPa at a shear strain rate of ~10^4 s^{-1}. The dominating measurement uncertainties, stemming from the VISAR resolution, are nearly constant and will remain virtually unchanged when applied to higher strength samples indicating that uncertainty will decrease on a percentage basis as the strength increases.

5.2. Proof-of-Principle Shot MS-11

The experimental configuration for shot MS-11, nearly identical experimental configuration to shot MS-10, is shown in Figure 40. This experiment utilized a thicker anvil on the bottom panel. Shot MS-11 was conducted with a reduced external B_o field to demonstrate that the results are independent of the external field strength providing sufficient shear is generated. The external magnetic field for this shot was 5.24 T resulting from a peak current of 5.61 kA from the MPG supply charged to 2.46 kV.

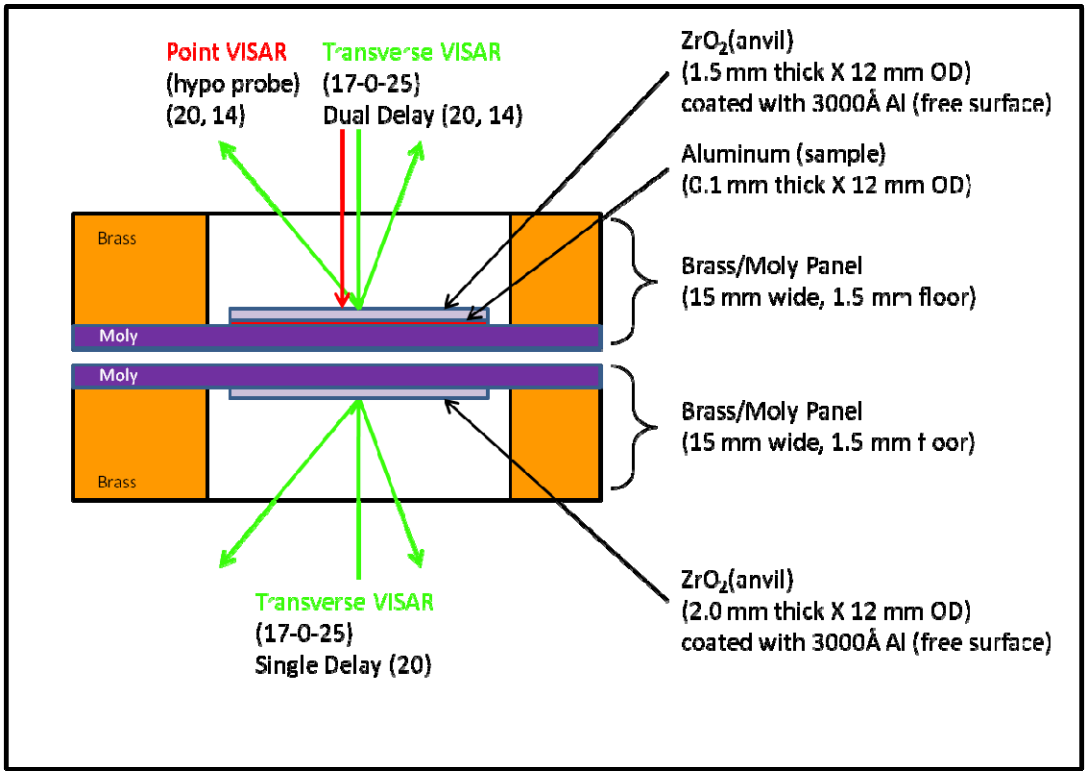

Figure 40: Experimental configuration for shot MS-11.

Apparent and resolved velocities are shown in Figure 41 and Figure 42 respectively. Comparison with the results of MS-10 indicates a reduction in shear wave velocity for the no sample case as expected as this is a measure of the generated shear. The shear wave velocity for the aluminum sample is also slightly reduced but within the experimental uncertainty is in agreement with that of shot MS-10. As mentioned previously, in order for an accurate probe of the sample yield strength, sufficient shear must be generated in the driver to reach yield in the sample. While the generated shear is similar to the yield strength of the sample in this case, observation of greater shear velocity for the no sample case than for the sample indicates that the shear wave was in fact truncated in the sample.

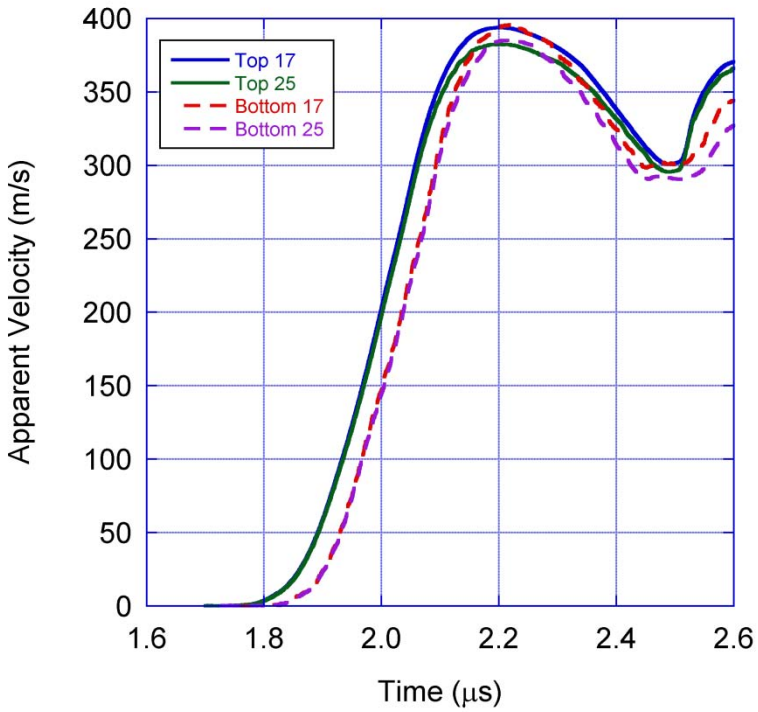

Figure 41: Apparent Apparent velocity recorded by the VISAR system for shot MS-11. Numbers in legend refer to the data collection probe angle. The top panel has an aluminum sample. The bottom panel has only the driver and anvil.

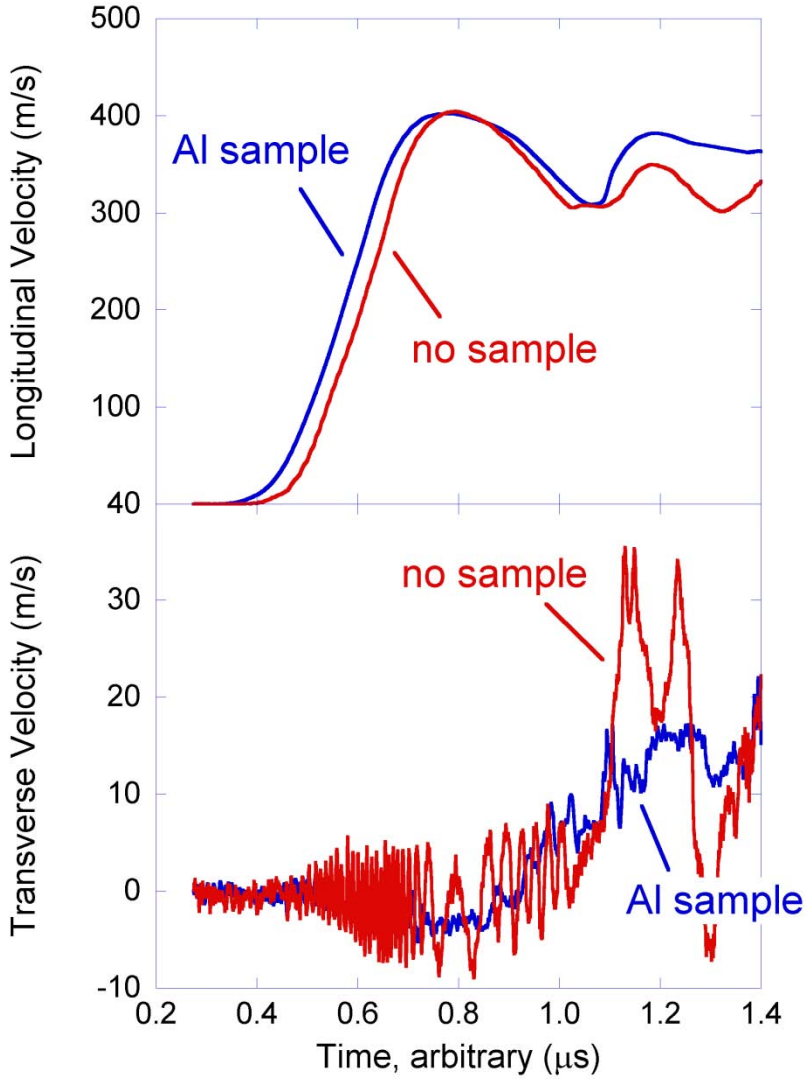

Figure 42: Resolved longitudinal and transverse velocities for shot MS-11.

The longitudinal and transverse free surface velocities were found to be 404.5 ± 3 m/s and 15.7 ± 3 m/s with the aluminum sample present and 399.3 ± 3 m/s and 32.0 ± 3 m/s without the sample. Following a similar methodology to the previous section, the yield strength of the sample was found to be 0.338 ± 0.047 GPa.

5.3. Anvil Characterization Shot MS-16

The results of MAPS experiments depend directly on the longitudinal and transverse wave speeds in the zirconia anvils. In order to provide the best possible results, these wave speeds were measured experimentally. The experimental configuration is shown in Figure 43. No samples are present and two different thickness zirconia anvils are used.

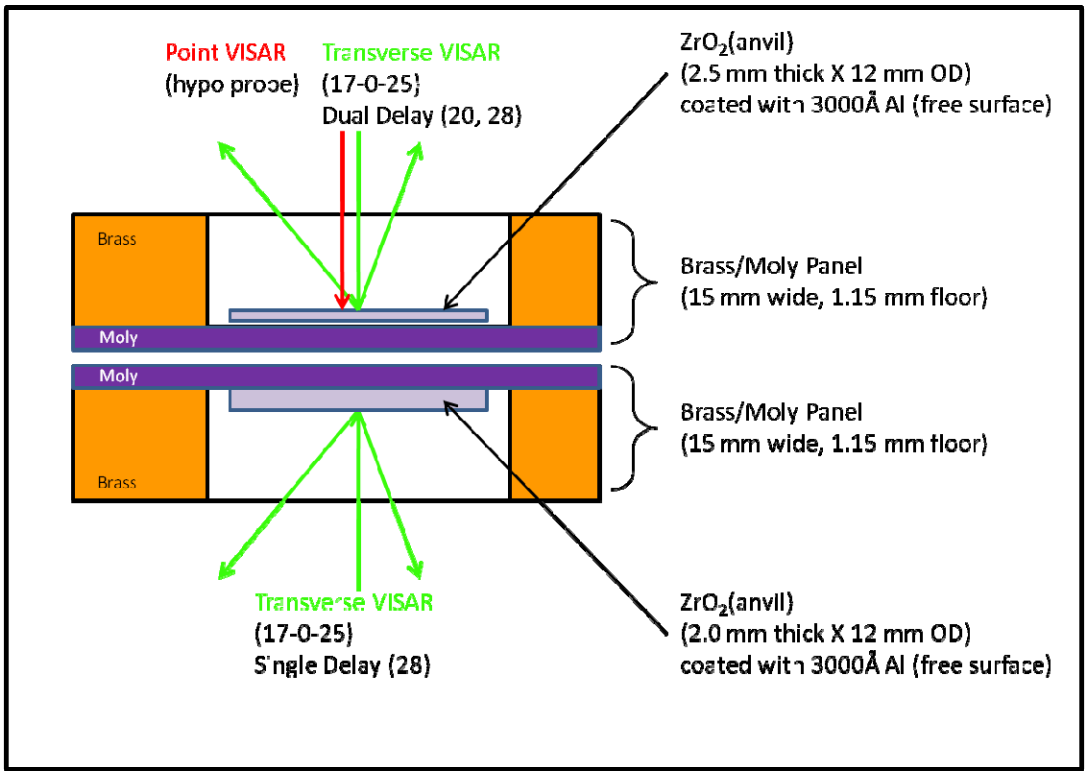

Figure 43: Experimental configuration for shot MS-16.

Resolved longitudinal and transverse velocities are shown in Figure 44. Longitudinal and transverse wave velocities can be determined by multiple analysis methods. The simplest approach is to consider the time difference, Δt, between the arrivals of each wave taken at the midpoint of the rise as shown in the figure for the longitudinal waves. Dividing the difference in anvil thicknesses by this change in arrival times results in an average wave speed in the anvils. Following this approach, the longitudinal wave speed, C_L, was found to be 7330 m/s and the transverse wave speed. C_S, was found to be 4105 m/s.

The wave speeds can also be determined by a characteristic analysis [37]. This approach determines the wave speed as a function of particle velocity or strain as opposed to only an average value. The determination of wave speed, especially for the shear wave, is complicated by the non-zero velocity recorded prior to the main shear arrival, especially for the 2.5 mm thick case. Preliminary results are shown in Figure 45. The linear fit to the longitudinal data ignored the large dip in the observed wave speed between u_p = 0.10 - 0.16 km/s. The validity of this

approach has not yet been determined. Note that the average values determined previously agree well with the characteristic results. For subsequent analysis, the average values were used.

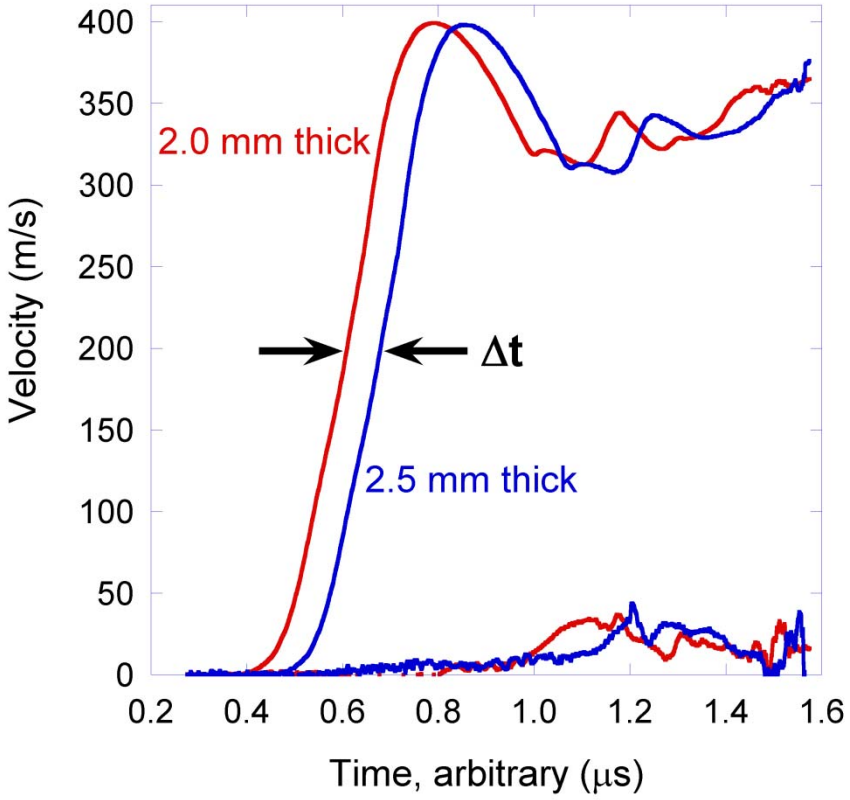

Figure 44: Resolved longitudinal and transverse velocity data from shot MS-16.

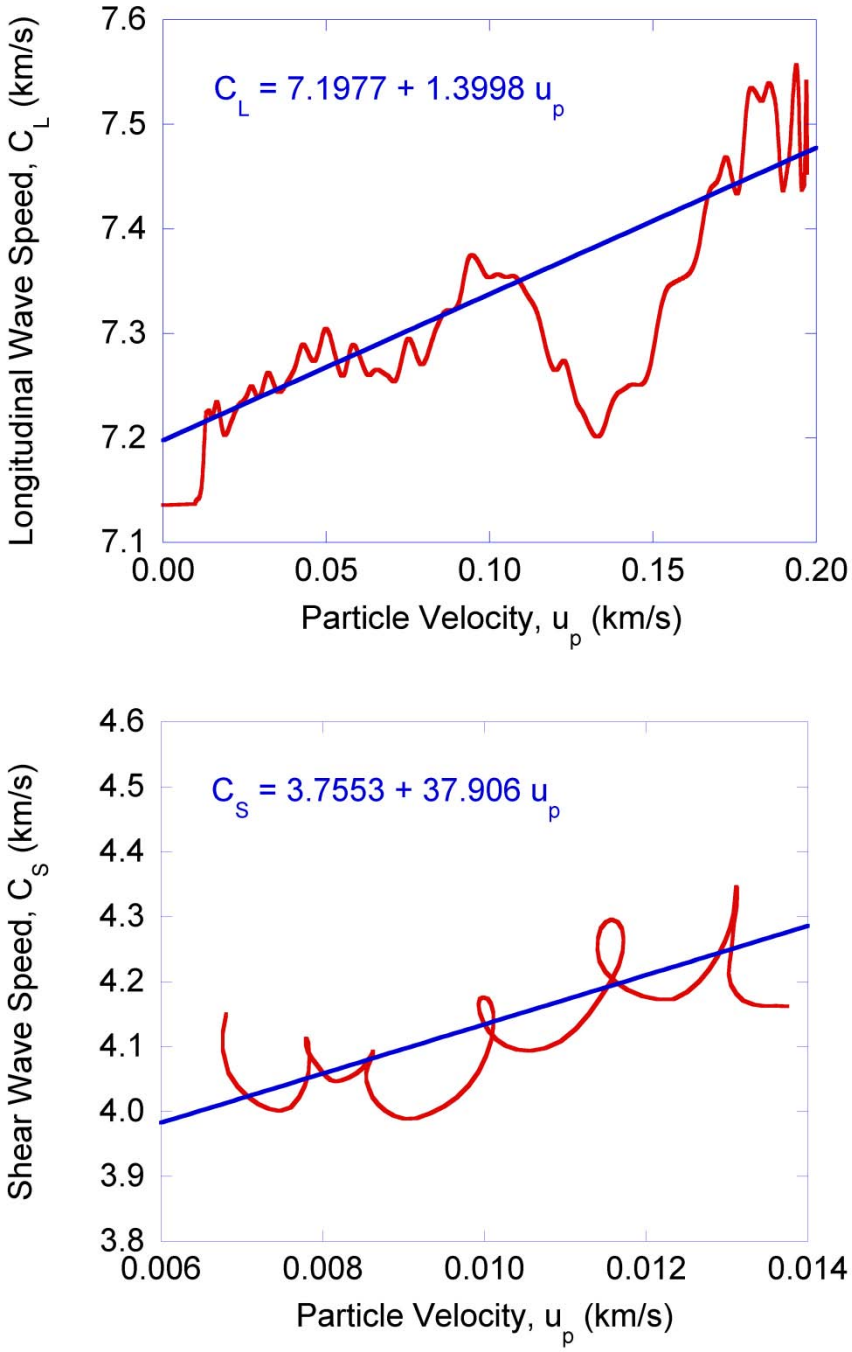

Figure 45: Longitudinal and shear wave speeds in zirconia determined from the wave profiles in Figure 44.

5.4. Comparison to published data and strength models

The results of the first two MAPS experiments, MS-10 and MS-11, are plotted as strength versus peak longitudinal stress in Figure 46. Also shown in the figure are results determined by the self-consistent method published by Huang and Asay [14, 38] and analytically determined strength values from both the Huang-Asay [14] and Steinberg-Guinan [12] models. Stress values for the MAPS data shown has been adjusted to account for differences between MAPS and the self-consistent methods. As discussed previously, MAPS data is collected in a pure shear state while the self-consistent approach determines strength for materials on the yield surface. As such, there is a small difference in the measured stress levels accounting for the difference $2/3Y_o$ between the hydrostat and the yield surface. For comparison to the previous results, this factor, which amounts to 0.24 GPa, was added to the MAPS results.

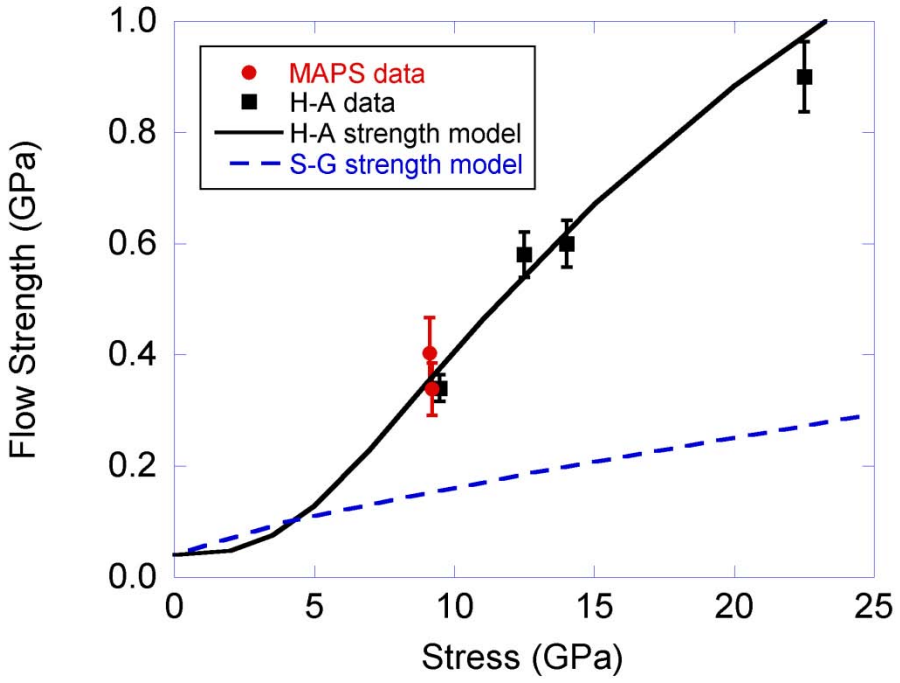

Figure 46: Strength of pure aluminum measured via the MAPS technique. Also shown are data from Huang and Asay13-14 for similar material. Curves show the predicted strength from the Huang-Asay (H-A)14 and Steinberg-Guinan (S-G)10 models. A slight correction of~0.24 GPa was applied to the MAPS measured longitudinal stress to be compatible with the previous data.

Data obtained via the new MAPS technique is more consistent with the Huang and Asay model. Further, the experimental uncertainty is sufficiently small to discriminate between the two strength models. Work is in progress to further refine this technique for better accuracy and to investigate the limits in stress and loading rate.

6. FUTURE WORK

6.1. Other materials

Following the success of MAPS measuring the strength in pure aluminum, the approach should be applied to other materials to verify the robustness of the technique. A range of materials with varying strengths should be measured. Potential candidates include tantalum and copper which have high and intermediate strengths respectively. Another interesting used of MAPS would be to study the yield strengths of aluminum alloys.

6.2. Model verification data

Material data under both pressure and shear loading, similar to that obtained on shot MS-16, provides an excellent test for existing and proposed computational models. Similar data collected on other materials could be quite useful to the modeling community. Even at the modest pressures attainable on Veloce, MAPS is capable of providing validation data. This unintended consequence could prove to be another valuable result.

6.3. Migration to Z

Ultimately, the MAPS technique will be most useful when used in conjunction with the Sandia Z machine. Z is capable of attaining much higher compression levels than Veloce and MAPS will be able to provide strength data at the multi-megabar pressures where strength is both unknown and critically important to DOE design issues.

Due to the similarities between a Z strip line geometry and the Veloce load design, minimal effort will be required to apply field MAPS on Z from the load perspective. However, similarly to the process of enabling the application of external magnetic fields on Veloce, this capability will be required on Z to utilize MAPS. A separate effort is in the process of designing and building the equivalent of the MPG system for use on Z. It is anticipated that the capability will be available on Z by late FY2011 or early FY2012.

6.4. PDV diagnostics

The majority of the current experimental uncertainty present in MAPS data is due to velocity measurement uncertainty. VISAR resolution on the scale of a few meters per second is exceptional performance for this device which is typically used for measuring velocities on the order of hundreds or thousands of meters per second. Photonic Doppler Velocimetry or PDV [39] is an alternative diagnostic that may e better suited to resolving small transverse velocities. A prototype PDV system is being modified to accommodate the passive/active probes required for transverse measurement capability and is expected to be available in FY11.

7. SUMMARY

This project achieved the goal of developing and demonstrating a new approach to measuring material strength using pulsed power MHD machines. The devised approach directly generates a

shear wave in the drive panel via interaction of the MHD drive current with an external magnetic field oriented normal to the drive current density. The usual longitudinal compression wave is unaffected by the external field. Thus, both pressure and shear are applied simultaneously via interaction with magnetic fields. For this reason the technique is referred to as magnetically applied pressure shear or MAPS. The MAPS technique further satisfied the wish that strength is directly determined from measurable quantities without the use of numeric models or simulation. Strength is probed by passing the shear wave through a sample material where the transmissible shear stress is limited to the sample strength. The magnitude of the transmitted shear wave is measured via a transverse VISAR system from which the sample strength is determined. Proof-of-principle tests were conducted on pure aluminum samples using the Veloce small pulser. MAPS strength data are in excellent agreement with existing data collected by other means.

REFERENCES

[1] Z. Tang and J. B. Aidun, in *Shock Wave Science and Technology Reference Library, Vol. 3*, edited by Y. Horie (Springer Berlin Heidelberg, 2009), pp. 1-59.

[2] J. R. Asay and J. Lipkin. A self-consistent technique for estimating the dynamic yield strength of a shock-loaded material. *Journal of Applied Physics*, 1978, **49**: 4242-4247.

[3] C. H. M. Simha and Y. M. Gupta. Time-dependent inelastic deformation of shocked soda-lime glass. *Journal of Applied Physics*, 2004, **96**(4): 1880-1890.

[4] G. R. Fowles. Shock wave compression of hardened and annealed 2024 aluminum. *Journal of Applied Physics*, 1961, **32**(8): 1475-1487.

[5] M. D. Furnish, L. C. Chhabildas and W. D. Reinhart. Time-resolved particle velocity measurements at impact velocities of 10 km/s. *International Journal of Impact Engineering*, 1999, **23**(1): 261-270.

[6] V. V. Igonin, O. N. Ignatova, A. I. Lebedev, M. O. Lebedeva, S. S. Nadezhin, A. M. Podurets, V. A. Raevsky, V. P. Solovyev, M. A. Zocher and D. L. Preston. Influence of Dynamic Properties on Perturbation Growth in Tantalum. *Shock Compression of Condensed Matter - 2009, Pts 1 and 2*, 2009, **1195**: 1085-1088.

[7] K. T. Lorenz, M. J. Edwards, S. G. Glendinning, A. F. Jankowski, J. McNaney, S. M. Pollaine and B. A. Remington. Accessing ultrahigh-pressure, quasi-isentropic states of matter. *Physics of Plasmas*, 2005, **12**(5): -.

[8] H. S. Park, K. T. Lorenz, R. M. Cavallo, S. M. Pollaine, S. T. Prisbrey, R. E. Rudd, R. C. Becker, J. V. Bernier and B. A. Remington. Viscous Rayleigh-Taylor Instability Experiments at High Pressure and Strain Rate. *Physical Review Letters*, 2010, **104**(13): -.

[9] F. J. Zerilli and R. W. Armstrong. Dislocation-Mechanics-Based Constitutive Relations for Material Dynamics Calculations. *Journal of Applied Physics*, 1987, **61**(5): 1816-1825.

[10] P. S. Follansbee and U. F. Kocks. A Constitutive Description of the Deformation of Copper Based on the Use of the Mechanical Threshold Stress as an Internal State Variable. *Acta Metallurgica*, 1988, **36**(1): 81-93.

[11] D. L. Preston, D. L. Tonks and D. C. Wallace. Model of plastic deformation for extreme loading conditions. *Journal of Applied Physics*, 2003, **93**(1): 211-220.

[12] D. J. Steinberg, S. G. Cochran and M. W. Guinan. A constitutive model for metals applicable at high-strain rate. *Journal of Applied Physics*, 1980, **51**: 1498-1504.

[13] W. A. Reinhart, J. R. Asay and C. S. Alexander. *in preperation*, 2010,

[14] H. Huang and J. R. Asay. Compressive strength measurements in aluminum for shock compression over the stress range of 4-22 GPa. *Journal of Applied Physics*, 2005, **98**(3): 033524.

[15] G. R. Johnson and W. H. Cook, "A constitutive model and data for metals subjected to large strains, high strain rates and high temperatures", presented at the 7th International Symposium on Ballistics Netherlands, 1983.

[16] M. K. Matzen. Z pinches as intense X-ray sources for high-energy density physics applications. *Physics of Plasmas*, 1997, **4**(5): 1519-1527.

[17] C. A. Hall. Isentropic compression experiments on the Sandia Z accelerator. *Physics of Plasmas*, 2000, **7**: 2069-2075.

[18] C. A. Hall, J. R. Asay, M. D. Knudson, W. A. Stygar, R. B. Spielman, T. D. Pointon, D. B. Reisman, A. Toor and R. C. Cauble. Experimental configuration for isentropic compression of solids using pulsed magnetic loading. *Review of Scientific Instruments*, 2001, **72**: 3587-3595.

[19] M. D. Knudsen and J.-P. Davis. 2010,

[20] T. Ao, J. R. Asay, S. Chantrenne, R. J. Hickman, M. D. Willis, A. W. Shay, S. A. Grine-Jones, C. A. Hall and M. R. Baer, The Veloce pulsed power generator for isentropic compression experiments, 2007.

[21] T. Ao, J. R. Asay, J. P. Davis, M. D. Knudson and C. A. Hall. High-pressure quasi-isentropic loading and unloading of interferometer windows on the veloce pulsed power generator. *Shock Compression of Condensed Matter - 2007, Pts 1 and 2*, 2007, **955**: 1157-1160.

[22] T. Ao, J. R. Asay, S. Chantrenne, M. R. Baer and C. A. Hall. A compact strip-line pulsed power generator for isentropic compression experiments. *Review of Scientific Instruments*, 2008, **79**(1): 013903-013901-013903-013903-013916.

[23] J. W. Swegle and L. C. Chhabildas, in *Shock Waves and High-Strain-Rate Phenomena in Metals*, edited by M. A. Meyers and L. E. Murr (Plenum Press, New York, 1981), pp. 401-415.

[24] A. C. Robinson, T. A. Brunner, S. Carroll, R. Drake, C. J. Garasi, H. Hanshaw, R. W. Lemke, E. Love, S. Mosso, J. Neiderhaus, C. Ober, S. Petney, W. J. Rider, G. Scovazzi, E. Strack, R. Summers, G. Weirs, M. Wong and T. Voth, ALEGRA : An Arbitrary

Lagrangian-Eulerian Multimaterial, Multiphysics Code, Report No. SAND2008-0038C, 2008.

[25] G. I. Kerley, CTH Reference Manual: The Equation of State Package, Report No. SAND98-0947, 1998.

[26] G. I. Kerley, CTH Reference Manual: The Steinberg-Guinan-Lund Viscoplastic Model, Report No. SAND92-0716, 1992.

[27] M. P. Desjarlais. Practical improvements to the Lee-More conductivity near the metal-insulator transition. *Contributions to Plasma Physics*, 2001, **41**(2-3): 267-270.

[28] M. P. Desjarlais, personal communication, 2009

[29] M. P. Desjarlais, J. D. Kress and L. A. Collins. Electrical conductivity for warm, dense aluminum plasmas and liquids. *Physical Review E*, 2002, **66**(2): -.

[30] M. Marder, SLINGSHOT – A Coilgun Design Code, Report No. SAND2001-1780, 2001.

[31] W. C. Young and R. G. Budynas, Roark's Formulas for Stress and Strain, 7th ed, Macgraw Hill, New York, 2002.

[32] Y. K. Huang, P. H. Frings and E. Hennes. Mechanical properties of Zylon/epoxy composite. *Composites Part B (Engineering)*, 2002, **33B**(2): 109-115.

[33] L. C. Chhabildas and J. W. Swegle. Dynamic pressure-shear loading of materials using anisotropic crystals. *Journal of Applied Physics*, 1980, **51**: 4799-4807.

[34] J. R. Robbins, personal communication, 2010

[35] J. R. Asay, T. Ao, T. J. Vogler, J. P. Davis and G. T. Gray. Yield strength of tantalum for shockless compression to 18 GPa. *Journal of Applied Physics*, 2009, **106**(7): -.

[36] D. E. Grady and T. Mashimo. Shock and Release Wave Properties of Yttria-Doped Tetragonal and Cubic Zirconia. *Journal of Applied Physics*, 1992, **71**(10): 4868-4874.

[37] T. Ao, IWA: an analysis program for isentropic wave measurements, Sandia Report No. SAND2009-0970, 2009.

[38] H. Huang and J. R. Asay. Reshock and release response of aluminum single crystal. *Journal of Applied Physics*, 2007, **101**(6): 063550.

[39] O. T. Strand, D. R. Goosman, C. Martinez, T. L. Whitworth and W. W. Kuhlow. Compact system for high-speed velocimetry using heterodyne techniques. *Review of Scientific Instruments*, 2006, **77**(8): 83108-83101-83108-83108-83108.

APPENDIX A

The following input deck was used to simulate experiment MS-10.

```
$ Aprepro (Revision: 2.06) Sat Aug 28 12:45:38 2010
$ FORMAT   = %.9g  $ default = "%.10g"

$ panel_h  = 0.02  $ panel height       [m]
$ panel_w  = 0.015  $ panel width        [m]

$ panel_t1 = 0.00115  $ panel thickness 1  [m]
$ panel_t2 = 0.0001  $ panel thickness 2  [m]
$ panel_t3 = 0.00156  $ panel thickness 3  [m]
$ panel_t  = 0.00281  $ total thickness    [m]

$ ak_gap   = 0.0005  $ gap between panels [m]
$ void     = 0.001  $ free surface void  [m]

$ dx       = 1e-05  $ cell size          [m]
$ dy       = 1e-05  $ cell size          [m]
$ ysym     = 50  $ symmetry factor

$ nx       = 431  $ number of cells
$ ny       = 30  $ number of cells

$ Bstatic  = 7.1  $ static B field     [T]
$ v_scale  = 1  $ current scaling factor

$ tmax     = 2.5e-06  $ termination time

$$$$$$$$$$$$$$$$$$$$$$$$$$$$$$$$$$$$$$$$$$$$$$$$$$$$$$$$$$$$$$$$$$$$$$$$$$$$$$$

title
Shear Panel, Width 15 mm, Layer 1 1.15 mm, Layer 2 0.1 mm, Layer 3 1.56 mm

$$$$$$$$$$$$$$$$$$$$$$$$$$$$ execution control $$$$$$$$$$$$$$$$$$$$$$$$$$$$$

  units, si
  copy input = false

  start time        = -0.10e-6
  termination time  =  2.5e-06

  emit screen,  cycle interval = 50
  emit output,  time  interval = 0.100e-6
  emit plot,    time  interval = 0.010e-6   $ from 0. to 1.
  emit hisplt,  time  interval = 0.001e-6   $ from 0. to 1.

$ termination cycle  =  25
$ emit screen,  cycle interval = 1
$ emit output,  cycle interval = 1
$ emit plot,    cycle interval = 1
$ emit hisplt,  cycle interval = 1

$ read restart dump, -1
$ emit restart, time  interval = 0.01e-6

  plot variable
    coordinates
    velocity
    velocity          : mag
    acceleration
    b
    b                 : mag
    jz
    ez
    ajxb
```

```
    density           : avg
    energy            : avg
    temperature       : avg
    pressure          : avg
    stress            : avg
    cauchy_stress     : avg
    dev_cauchy_stress : avg
    yield_stress      : avg
    sound speed       : avg
    specific heat vol : avg
    econ              : avg
    thermal con       : avg
    zbar              : avg
    artificial viscosity
  end

  history plot variable
    no material globals
    coordinates
    velocity
    velocity          : mag
    acceleration
    b
    b                 : mag
    jz
    ez
    ajxb
    density           : avg
    energy            : avg
    temperature       : avg
    pressure          : avg
    sound speed       : avg
    specific heat vol : avg
    econ              : avg
    thermal con       : avg
    zbar              : avg

    stress            : avg
    cauchy_stress     : avg
    dev_cauchy_stress : avg
    shear_modulus     : avg
    yield_stress      : avg
    plas_strn_rate    : avg
    eqps              : avg

    artificial viscosity
  end

$$$$$$$$$$$$$$$$$$$$$$$$$$$$$$ physics options $$$$$$$$$$$$$$$$$$$$$$$$$$$$$$

  magnetohydrodynamics conduction
    cartesian, 2D
    volumetric scale factor 50 $ symmetry
               scale length 0.02 $ scale length
    detailed energy tallies

    max init time step = 1.0e-09

    mesh, inline
      brick
        numx 5
          xblock 1  0.0005  first size 1e-05
          xblock 2  0.00115  first size 1e-05
          xblock 3  0.0001  first size 5e-06
          xblock 4  0.00156  first size 1e-05
          xblock 5  0.001  first size 1e-05
        numy 1
          yblock 1  0.0003  first size 1e-05
      end
      set assign
```

```
    nodeset, ilo, 11  $ left   (-x)
    nodeset, ihi, 12  $ right  (+x)
    nodeset, jlo, 21  $ bottom (-y)
    nodeset, jhi, 22  $ top    (+y)

    sideset, ilo, 11  $ left   (-x)
    sideset, ihi, 12  $ right  (+x)
    sideset, jlo, 21  $ bottom (-y)
    sideset, jhi, 22  $ top    (+y)
  end
end

$ lower left at (0,0)
$ so do not need to shift mesh
$ arbitrary map mesh,
$   "newpos[0] = oldpos[0] + 0.002155;"

hydrodynamics
$ void compression      = off     $ default = off

  no displacement, nodeset 11, x  $ left   (-x)
  no displacement, nodeset 12, x  $ right  (+x)

$ no displacement, nodeset 21, y  $ bottom (-y)
$ no displacement, nodeset 22, y  $ top    (+y)

  periodic bc,     nodeset 21
                   translate,
                   x 0.
                   y 0.0003
                   nodeset 22
end

transient magnetics
  initial b field,  mean,        $ static applied field
                    x 7.1
                    y 0.

$ b field applied at left side in ak gap
$ function 1 = specifies total current
$ scale      = adjusts for finite angle and width

  uniform h bc, sideset 11        $ left   (-x)
                function 1        $ total current
                scale 0.85        $ account for edge effects
                x 0.  y -1.       $ tangent
                length 0.015  $ convert I to B

  uniform h bc, sideset 12        $ left   (+x)
                function 1        $ total current
                scale 0.          $ zero field
                x 0.  y 1.        $ tangent
                length 0.015  $ convert I to B

  current tally, 1, block 1, sym fac 50,   $ symmetry
                    block 2, sym fac 50,   $ symmetry
                    block 3, sym fac 50,   $ symmetry
                    block 4, sym fac 50,   $ symmetry
                    block 5, sym fac 50,   $ symmetry
                    end

  insulator material = 3 4
  joule heat, maxsig  $ default = standard
  aztec set,  1

$ DICE 52 current profile
  include "Veloce_Shot_52.dat"
end

thermal conduction
```

```
  scale 1.e20
  no heat flux, sideset 11    $ left   (-x)
  no heat flux, sideset 12    $ right  (+x)
  no heat flux, sideset 21    $ bottom (-y)
  no heat flux, sideset 22    $ top    (+y)
end

block 1         $ ak gap
  eulerian mesh
end

block 2         $ panel
  eulerian mesh
  material 1
end

block 3         $ panel
  eulerian mesh
  material 2
end

block 4         $ panel
  eulerian mesh
  material 3
end

block 5         $ void
  eulerian mesh
end

$ atracer  = 57.5  $ number of tracers
$ btracer  = 20  $ number of tracers
$ ctracer  = 78  $ number of tracers

$ adx      = 2e-05  $ spacing of tracers
$ bdx      = 5e-06  $ spacing of tracers
$ cdx      = 2e-05  $ spacing of tracers

$ aloc     = 0.0005  $ start of tracer points
$ bloc     = 0.00165  $ start of tracer points
$ cloc     = 0.00175  $ start of tracer points

$ acnt     = -1  $ count of tracer points
$ bcnt     = -1  $ count of tracer points
$ ccnt     = -1  $ count of tracer points

tracer points
  lag tracer 100  x 0.00051  y 5e-06
  lag tracer 101  x 0.00053  y 5e-06
  lag tracer 102  x 0.00055  y 5e-06
  lag tracer 103  x 0.00057  y 5e-06
  lag tracer 104  x 0.00059  y 5e-06
  lag tracer 105  x 0.00061  y 5e-06
  lag tracer 106  x 0.00063  y 5e-06
  lag tracer 107  x 0.00065  y 5e-06
  lag tracer 108  x 0.00067  y 5e-06
  lag tracer 109  x 0.00069  y 5e-06
  lag tracer 110  x 0.00071  y 5e-06
  lag tracer 111  x 0.00073  y 5e-06
  lag tracer 112  x 0.00075  y 5e-06
  lag tracer 113  x 0.00077  y 5e-06
  lag tracer 114  x 0.00079  y 5e-06
  lag tracer 115  x 0.00081  y 5e-06
  lag tracer 116  x 0.00083  y 5e-06
  lag tracer 117  x 0.00085  y 5e-06
  lag tracer 118  x 0.00087  y 5e-06
  lag tracer 119  x 0.00089  y 5e-06
  lag tracer 120  x 0.00091  y 5e-06
  lag tracer 121  x 0.00093  y 5e-06
  lag tracer 122  x 0.00095  y 5e-06
```

```
lag tracer 123  x 0.00097  y 5e-06
lag tracer 124  x 0.00099  y 5e-06
lag tracer 125  x 0.00101  y 5e-06
lag tracer 126  x 0.00103  y 5e-06
lag tracer 127  x 0.00105  y 5e-06
lag tracer 128  x 0.00107  y 5e-06
lag tracer 129  x 0.00109  y 5e-06
lag tracer 130  x 0.00111  y 5e-06
lag tracer 131  x 0.00113  y 5e-06
lag tracer 132  x 0.00115  y 5e-06
lag tracer 133  x 0.00117  y 5e-06
lag tracer 134  x 0.00119  y 5e-06
lag tracer 135  x 0.00121  y 5e-06
lag tracer 136  x 0.00123  y 5e-06
lag tracer 137  x 0.00125  y 5e-06
lag tracer 138  x 0.00127  y 5e-06
lag tracer 139  x 0.00129  y 5e-06
lag tracer 140  x 0.00131  y 5e-06
lag tracer 141  x 0.00133  y 5e-06
lag tracer 142  x 0.00135  y 5e-06
lag tracer 143  x 0.00137  y 5e-06
lag tracer 144  x 0.00139  y 5e-06
lag tracer 145  x 0.00141  y 5e-06
lag tracer 146  x 0.00143  y 5e-06
lag tracer 147  x 0.00145  y 5e-06
lag tracer 148  x 0.00147  y 5e-06
lag tracer 149  x 0.00149  y 5e-06
lag tracer 150  x 0.00151  y 5e-06
lag tracer 151  x 0.00153  y 5e-06
lag tracer 152  x 0.00155  y 5e-06
lag tracer 153  x 0.00157  y 5e-06
lag tracer 154  x 0.00159  y 5e-06
lag tracer 155  x 0.00161  y 5e-06
lag tracer 156  x 0.00163  y 5e-06

lag tracer 200  x 0.0016525  y 5e-06
lag tracer 201  x 0.0016575  y 5e-06
lag tracer 202  x 0.0016625  y 5e-06
lag tracer 203  x 0.0016675  y 5e-06
lag tracer 204  x 0.0016725  y 5e-06
lag tracer 205  x 0.0016775  y 5e-06
lag tracer 206  x 0.0016825  y 5e-06
lag tracer 207  x 0.0016875  y 5e-06
lag tracer 208  x 0.0016925  y 5e-06
lag tracer 209  x 0.0016975  y 5e-06
lag tracer 210  x 0.0017025  y 5e-06
lag tracer 211  x 0.0017075  y 5e-06
lag tracer 212  x 0.0017125  y 5e-06
lag tracer 213  x 0.0017175  y 5e-06
lag tracer 214  x 0.0017225  y 5e-06
lag tracer 215  x 0.0017275  y 5e-06
lag tracer 216  x 0.0017325  y 5e-06
lag tracer 217  x 0.0017375  y 5e-06
lag tracer 218  x 0.0017425  y 5e-06
lag tracer 219  x 0.0017475  y 5e-06

lag tracer 300  x 0.00176  y 5e-06
lag tracer 301  x 0.00178  y 5e-06
lag tracer 302  x 0.0018  y 5e-06
lag tracer 303  x 0.00182  y 5e-06
lag tracer 304  x 0.00184  y 5e-06
lag tracer 305  x 0.00186  y 5e-06
lag tracer 306  x 0.00188  y 5e-06
lag tracer 307  x 0.0019  y 5e-06
lag tracer 308  x 0.00192  y 5e-06
lag tracer 309  x 0.00194  y 5e-06
lag tracer 310  x 0.00196  y 5e-06
lag tracer 311  x 0.00198  y 5e-06
lag tracer 312  x 0.002  y 5e-06
lag tracer 313  x 0.00202  y 5e-06
```

```
      lag tracer 314  x 0.00204  y 5e-06
      lag tracer 315  x 0.00206  y 5e-06
      lag tracer 316  x 0.00208  y 5e-06
      lag tracer 317  x 0.0021  y 5e-06
      lag tracer 318  x 0.00212  y 5e-06
      lag tracer 319  x 0.00214  y 5e-06
      lag tracer 320  x 0.00216  y 5e-06
      lag tracer 321  x 0.00218  y 5e-06
      lag tracer 322  x 0.0022  y 5e-06
      lag tracer 323  x 0.00222  y 5e-06
      lag tracer 324  x 0.00224  y 5e-06
      lag tracer 325  x 0.00226  y 5e-06
      lag tracer 326  x 0.00228  y 5e-06
      lag tracer 327  x 0.0023  y 5e-06
      lag tracer 328  x 0.00232  y 5e-06
      lag tracer 329  x 0.00234  y 5e-06
      lag tracer 330  x 0.00236  y 5e-06
      lag tracer 331  x 0.00238  y 5e-06
      lag tracer 332  x 0.0024  y 5e-06
      lag tracer 333  x 0.00242  y 5e-06
      lag tracer 334  x 0.00244  y 5e-06
      lag tracer 335  x 0.00246  y 5e-06
      lag tracer 336  x 0.00248  y 5e-06
      lag tracer 337  x 0.0025  y 5e-06
      lag tracer 338  x 0.00252  y 5e-06
      lag tracer 339  x 0.00254  y 5e-06
      lag tracer 340  x 0.00256  y 5e-06
      lag tracer 341  x 0.00258  y 5e-06
      lag tracer 342  x 0.0026  y 5e-06
      lag tracer 343  x 0.00262  y 5e-06
      lag tracer 344  x 0.00264  y 5e-06
      lag tracer 345  x 0.00266  y 5e-06
      lag tracer 346  x 0.00268  y 5e-06
      lag tracer 347  x 0.0027  y 5e-06
      lag tracer 348  x 0.00272  y 5e-06
      lag tracer 349  x 0.00274  y 5e-06
      lag tracer 350  x 0.00276  y 5e-06
      lag tracer 351  x 0.00278  y 5e-06
      lag tracer 352  x 0.0028  y 5e-06
      lag tracer 353  x 0.00282  y 5e-06
      lag tracer 354  x 0.00284  y 5e-06
      lag tracer 355  x 0.00286  y 5e-06
      lag tracer 356  x 0.00288  y 5e-06
      lag tracer 357  x 0.0029  y 5e-06
      lag tracer 358  x 0.00292  y 5e-06
      lag tracer 359  x 0.00294  y 5e-06
      lag tracer 360  x 0.00296  y 5e-06
      lag tracer 361  x 0.00298  y 5e-06
      lag tracer 362  x 0.003  y 5e-06
      lag tracer 363  x 0.00302  y 5e-06
      lag tracer 364  x 0.00304  y 5e-06
      lag tracer 365  x 0.00306  y 5e-06
      lag tracer 366  x 0.00308  y 5e-06
      lag tracer 367  x 0.0031  y 5e-06
      lag tracer 368  x 0.00312  y 5e-06
      lag tracer 369  x 0.00314  y 5e-06
      lag tracer 370  x 0.00316  y 5e-06
      lag tracer 371  x 0.00318  y 5e-06
      lag tracer 372  x 0.0032  y 5e-06
      lag tracer 373  x 0.00322  y 5e-06
      lag tracer 374  x 0.00324  y 5e-06
      lag tracer 375  x 0.00326  y 5e-06
      lag tracer 376  x 0.00328  y 5e-06
      lag tracer 377  x 0.0033  y 5e-06

      lag tracer 500  x 0.003305  y 5e-06
    end
  end

$$$$$$$$$$$$$$$$$$$$$$$$$$$$$$ algorithm control $$$$$$$$$$$$$$$$$$$$$$$$$$$$$$
```

```
  aztec 0     $ thermal conduction control
    tol       = 1.e-14    $ default = 1.e-12
    max iter  = 1000      $ default = 500
    output    = none      $ default = none
  end

  aztec 1     $ transient magnetics control
$   solver    = lu        $ default = cg
    solver    = cg        $ default = cg
    scaling   = sym_diag  $ default = sym_diag
    precond   = sym_gs    $ default = none
    conv norm = rhs       $ default = r0
    tol       = 1.e-14    $ default = 1.e-12
    max iter  = 1000      $ default = 500
    output    = none      $ default = none
  end

$$$$$$$$$$$$$$$$$$$$$$$$$$$$$$ material models $$$$$$$$$$$$$$$$$$$$$$$$$$$$$$

  material 1  "Molybdenum"
    model  = 10                 $ EOS + elastic/plastic
    model  = 13                 $ electrical/thermal conductivity
  end

  model 10 cth elastic plastic   $ cth elastic plastic
    eos model     = 11
    yield model   = 12
  $ yield stress  =  1.6000e+09
  $ poisson ratio =  3.7500e-01

    phase control       = 1
    phasec noresolidify = 1
    $ phasec tmelt      = lindemann melt law
    $ phasec rhomin     = 0.8 * rhosolid
  end

  model 11 keos sesame          $ Mo EOS
    matlabel = 'MOLYBDENUM'
  $ neos     = 2984
  $ feos     = 'aneos'
    loclip   = 100.             $ K
  end

  model 12 steinberg guinan lund $ yield model
    matlabel = 'MOLYBDENUM'     $ 'Mo'
  end

  model 13 lmd                  $ Mo conductivity
    z         = 42.             $ Molybdenum
  end

$$$$$$$$$$$$$$$$$$$$$$$$$$$$$$ material models $$$$$$$$$$$$$$$$$$$$$$$$$$$$$$

  material 2  "Al 6061-T6"
    model  = 20                 $ EOS + elastic/plastic
    model  = 23                 $ electrical/thermal conductivity
  end

  model 20 cth elastic plastic   $ cth elastic plastic
    eos model     = 21
    yield model   = 22
  $ yield stress  =  0.2900e+09
  $ poisson ratio =  3.3000e-01

    phase control       = 1
    phasec noresolidify = 1
    $ phasec tmelt      = lindemann melt law
    $ phasec rhomin     = 0.8 * rhosolid
  end
```

```
  model 21 snl sesame            $ Al EOS
  $ feos       = 'al3720.asc'
    nmat       = 3720
    table      = 301
    min temper = 100.            $ K
  end

  model 22 steinberg guinan lund $ yield model
    matlabel = '6061-T6_ALUMINUM'
  end

  model 23 lmd                   $ Al conductivity
    z         = 13.
  end

$$$$$$$$$$$$$$$$$$$$$$$$$$$$$$ material models $$$$$$$$$$$$$$$$$$$$$$$$$$$$$$

  material 3  "Zirconia"
    model = 30                   $ EOS + elastic/plastic
    model = 33                   $ electrical/thermal conductivity
  end

  $ nu  = 0.3177     $ Poissons ratio
  $ hel = 16     $ Hugoniot elastic limit [GPa]
  $ y0  = 8.54990473     $ Yield strength
  model 30 cth elastic plastic   $ cth elastic plastic
    eos model     = 31
  $ yield model   = 32           $ No yield model means elastic-perfectly plastic
    yield stress  = 8.54990473e+09     $ Pa
    poisson ratio = 0.3177
  end

  $ parameters from:
  $   Grady & Mashimo, JAP, 71 (10) 4868, May 1992
  $   Mashimo, et al., JAP, 77 (10) 5069, May 1995
  model 31 mg us up              $ EOS
    gamma0  = 1.93
    c0      = 5.64e3             $ m/s
  $ sl      = 2.09               $ first wave
    sl      = 1.75               $
    cv      = 0.5228e3           $ J/kg/K
  $ rho ref = 5.954e3            $ kg/m^3
    rho ref = 6.028e3            $ kg/m^3
    tref    = 298.0              $ K
    pref    = 1.01e5             $ Pa (N/m^2)
    eref    = 0.0                $ J/kg
  end

$ model 32 steinberg guinan lund $ yield model
$   matlabel = 'ZIRCONIUM'       $ this is not 'ZrO2'
$ end

  model 33 ec knoepfel           $ ZrO2 conductivity
    sigma0    = 1.e-6            $ set conductivity = background conduct.
  end

$$$$$$$$$$$$$$$$$$$$$$$$$$$$$$ the end $$$$$$$$$$$$$$$$$$$$$$$$$$$$$$$$

  check shutdown file = 1m
  exit
```

DISTRIBUTION

5	MS1195	Scott Alexander	1646
1	MS1195	Tom Ao	1646
1	MS1195	Jim Asay	1646
1	MS1195	Lalit Chhabildas	1646
1	MS1195	Jean-Paul Davis	1646
1	MS1195	Jow-Lian Ding	1646
1	MS1195	Dan Dolan	1646
1	MS1195	Mike Furnish	1646
1	MS1195	Randy Hickman	1646
1	MS1195	Marcus Knudson	1646
1	MS1195	Bill Reinhart	1646
1	MS1195	Seth Root	1646
1	MS1195	Jack Wise	1646
1	MS0378	John Niederhaus	1431
1	MS0378	Greg Weirs	1431
1	MS1186	Mike Desjarlais	1640
1	MS1186	Mark Herrmann	1640
1	MS1189	Dawn Flicker	1641
1	MS1189	Tom Haill	1641
1	MS1193	Dean Rovang	1643
1	MS1191	John Porter	1670
1	MS1193	Briggs Atherton	1672
1	MS1182	Ron Kaye	5445
1	MS1182	Derek Lamppa	5445
1	MS1205	Clint Hall	5902
1	MS9042	Tracy Vogler	8246
1	MS0359	Donna L. Chavez	1911 (electronic copy)
1	MS0899	Technical Library	9536 (electronic copy)

Thomas A Mehlhorn
Superintendent, Plasma Physics Division
U.S. Naval Research Laboratory
Code 6700 (Bldg 101, Room 123)
4555 Overlook Ave. SW
Washington, DC 20375


Sandia National Laboratories